POLITECNICO
DI TORINO

Experimental Investigation of Hydrodynamic Cavitation using High Speed Visualization

OCTOBER 17, 2018

Continetal AG, OTH Regensburg, Politecnico di Torino

Experimental Investigation of Hydrodynamic Cavitation using High Speed Visualization.

Student Name: **GITAU STEPHEN**

To obtain a Master's Degree in Mechanical Engineering at Politecnico di Torino.

Supervisors:

M.Sc. H. Markus

Prof. M. Pfitzner

Dr. U. Leuteritz

Dr. HP Rabl

Prof. Daniela Misul

Institutions**: Continental AG, OTH Regensburg, Politecnico di Torino.**

Acknowledgement

I would like to thank my Supervisors for their different supports provided throughout the period of this thesis. In particular, I would like to thank Mr. Markus Hosbach for his patience and guidance in every step through the project. I learnt a lot working with him every day. Many Thanks!

I would also like to thank Mr. Uwe Leuteritz as the supervisor from Continental AG, for the opportunity to be part of this project and his support in providing everything needed to complete the project. I would also like to thank Mr. Rabl for being my coordinator at OTH Regensburg.

I am grateful to Miss. Misul for accepting to be my main and grading Supervisor at Politecnico di Torino. Thank you for showing interest in the project and for the full year of coursework I did with you.

A very special gratitude goes to my main University, Politecnico di Torino, for providing me with the opportunity and the chance to work on this project abroad.

TABLE OF CONTENTS

Abstract

This project initiated from ongoing research on erosion in microchannels due to aggressive cavitation. Aggressive cavitation is a major concern when designing tools that apply high velocity fluid dynamics. The approach of this thesis is to develop a concept for a setup rig to visually investigate cavitation in micro channels. The developed concept will be set up and experimental tests on 2D channels will be done. The aim is to understand the effect of different parameters on cavitation mechanism. This will give more insight on the internal structures of cavitation and how this structures translate to erosion results found in the past and ongoing erosion research. Cavitation also has influence on fuel atomization and the whole process of combustion, emission and performance are affected by injection. Thus, the findings will of this thesis will be applied in understanding the dynamics during injection in fuel injectors.

Different microchannel geometries will be tested under different operating conditions. High-speed videos will be used to characterize the high velocity kinematics of cavitation structures. Image analysis techniques will be applied to process the high-speed videos and then non-dimensional analysis will be used to generalize the findings. Strouhal number, Reynolds number, normalized lengths and Cavitation number among other parameters will be used.

Nomenclature

f	*Shedding frequency*
g	*Gravitational acceleration*
h	*Microchannel height*
L	*Microchannel length*
l	*Length of cavity*
p	*Pressure*
Δp	*Pressure difference*
r	*Bubble/ cavity radius*
Re	*Reynolds number*
str	*Strouhal number*
T	*Temperature*
t_o	*Reference time*
Δt	*Images interframe time*
v	*Velocity*
z	*Hydraulic head*
σ	*Cavitation number*
τ	*Exposure time/laser pulse duration*
μ	*Kinematic viscosity*
γ	*Specific weight*
ρ	*Density*

1 INTRODUCTION AND THEORETICAL STUDY

Cavitation is a phenomenon that occurs when bubbles or cavities form in an initially homogenous fluid due to the pressure being lower than the vapor pressure of that fluid. Cavitation occurrence was first observed by an Irish fluid dynamics innovator called *Osborne Reynolds*. In today's world a very close understanding of cavitation is fundamental because it affects a wide range of engineering simulations and engineering designs.

Cavitation can happen both in static and dynamic conditions in fluids. Essentially when cavitation happens bubbles form, grow and propagate and finally collapse releasing great spasms of energy. When cavitation collapse happens close to a solid surface, erosion can occur. This is why when designing engineering tools which come into direct contact with fluids at low pressure it is important to account for cavitation, try to reduce it or increase it depending on the desired function. Head losses and rapid acceleration or relative acceleration, which can be caused by a vessel geometry or reduction in cross-sectional area, can lead to low pressure. It is characterized by a cracking sound. These audible and visible signs, along with damage in the form of erosion to a solid surface, are the most recognizable aspects of cavitation. There are two categories of cavitation, vaporous cavitation and gaseous cavitation. Vaporous cavitation is when the bubbles are filled with vapor while gaseous cavitation is when the bubbles are filled with gasses that are already dissolved in the liquid. Cavity structures in this case develop by mass diffusion of the gasses in the liquid.

The concept that an increase in velocity of a fluid or the increase in the altitude leads to a decrease in pressure can be demonstrated by the Bernoulli's Equation:

$$\frac{P_1}{\gamma} + \frac{V_1^2}{2g} + z_1 = constant(C) \qquad (1.1)$$

P_1 is the pressure at a defined point in the flow, γ is the specific weight of fluid , V_1 is the velocity at that point in the fluid, g represents the gravity, z_1 the vertical height where the fluid operates at and Bernoulli equation states that at any point the sum of these components is constant (C). If we apply this

equation in the case of a horizontal venturi nozzle (see fig 1.1), we can reduce the equation by assuming that the hydraulic head z_1 is constant and negligible

$$\frac{P_1}{\gamma} + \frac{V_1^2}{2g} = C \implies P_1 = \left(C - \frac{V_1^2}{2g}\right) \cdot \gamma \tag{1.2}$$

equation 1.2 shows a negative relation between the pressure and the relative velocity of a liquid, as the velocity increases the pressure decreases.

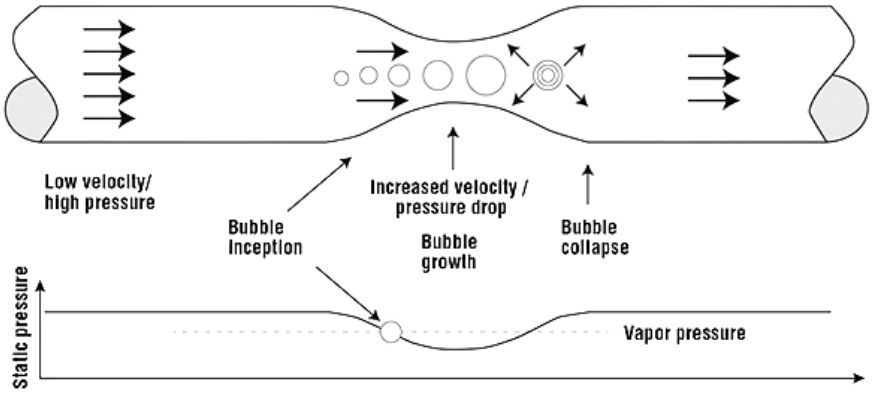

Fig. 1.1 Schematic of the pressure and velocity during the occurrence of cavitation in a venturi nozzle.

As demonstrated on the diagram (see fig. 1.1), when the cross sectional area of the flow is reduced, conservation of mass stipulates there will be an increase in the velocity of the liquid. With equation 1.2 an increase in the velocity reduces the pressure. If significantly reduced, it could get lower than the vapour pressure of the liquid and cavitation happens (see fig.1.2). At a first instance cavitation can be confused with boiling, except that cavitation is controlled by inertia and pressure forces while boiling is controlled by temperatures (see fig.1.2).

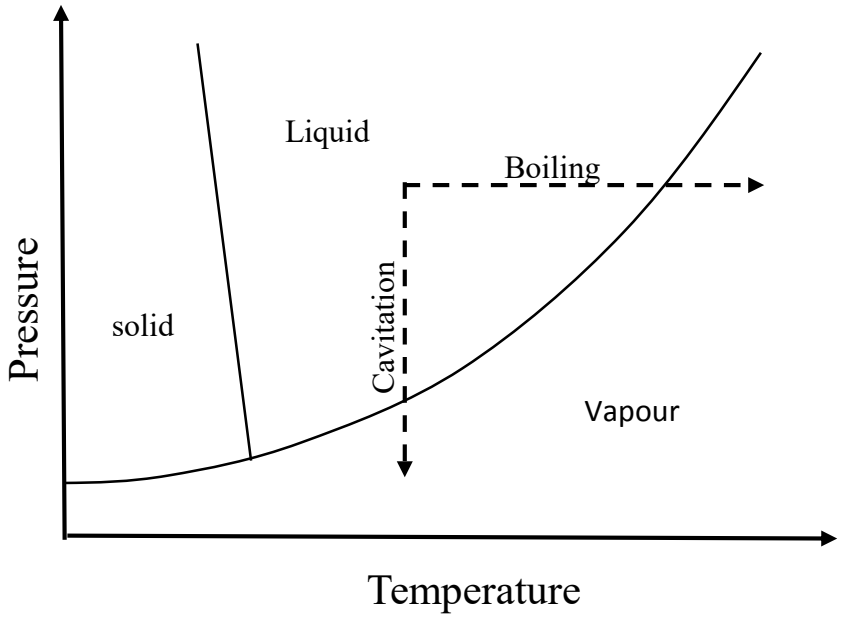

Fig. 1.2 A Pressure-Temperature phase diagram depicting the process of cavitation and boiling

1.1 HYDRODYNAMIC CAVITATION.

This describes the process of formation of vapor bubbles, the growth and eventual implosion of the bubbles. Bubbles and cavities form due to reduction of local pressures to a value below the vapor pressure and subsequent recovery of the pressure causes the implosion. Usually this happens when a fluid is passed through narrow or constricted channels or by mechanical movement or rotation of objects through a liquid. Many researches have associated this kind of cavitation with high level of aggressiveness which can be very destructive. Due to the wear and damage caused by cavitation, most effort is put towards avoiding it but it is important to note that if controlled, the high energy during the collapse of these cavities can be harnessed, for example if cavitation is used to clean biomedical equipment. Controlled cavitation can be useful to improve the performance of high speed vessels or projectiles for example by super-cavitation. It may play a beneficial role in the particular case of fuel injection, by enhancing atomization processes or reducing nozzle fouling.

In hydrodynamic cavitation, as introduced before, cavitation occurs basically when the local tension $P_v - P$ exceeds the tensile strength of the fluid, $P_v - P_{cr}$ [18]. Where P_v is the vapour pressure, P and P_{cr} are the local pressure and critical pressure respectively. Cavitation initiation mainly depends on the nucleation sites, which are areas of weakness in the liquid. When the equilibrium between the various

forces acting on the nuclei cannot balance, cavitation happens. Once cavities form in a homogenous liquid, the continuity of the liquid should be broken; therefore, the necessary pressure is determined not by the pressure of the saturated vapor but by the tensile strength of the liquid at the given temperature [1]. Methods of estimating the tensile strength of liquids include the theory internal pressure, which focuses on the interaction of van-der-Waals intermolecular forces, proposed by Temperly in 1947 [19].

1.2 BUBBLE DYNAMICS

Need for understanding the phenomena of cavitation has captured the attention of researchers who are after a good understanding of the formation, flow and collapse of bubbles during cavitation. Experimental and numerical research has been applied to investigate the formation and collapse or single bubbles.

Rayleigh (1978) developed the pressure dynamic theory for the collapse of the bubble, and developed what is known as the Rayleigh equation. Many researchers have used this equation and this theory to develop more complex theories in this field of bubble and cloud propagation in liquid. *Plesset* (1948) further considered the introduction of physical traits of the liquid like fluid viscosity and the liquid's surface tension (Yang, Jaw and Yeh [15]).

Gilmore (1952) moved forward to introduce the compressibility of the liquid on the flow field of the bubble collapse. *Plesset* and *Zwick* (1952) furthered the research to include the influence of thermos conductivity on the fluid flow of the bubble collapse. According to this research the time required for the bubble collapse is too short and the thermos conductivity influence is too, therefore, it can be entirely considered as an adiabatic process.

Rayleigh (1917) first analyzed the theoretical pressure variation of the flow field of the bubble collapse. The bubble collapse results in very high pressure, forming a shock wave which is sent toward the outside of the bubble. *Harrison* (1952) in his experimental results proved the existence of noise generated by the collapse of a bubble at its surrounding solid boundary. *Vogel* and *Lauterborn* (1988) found a close relationship between the strength of the wave pulse and the distance between the bubble and the solid boundary. This wave pulse could then generate a series of shock waves [15]

1.3 RAYLEIGH-PLESSET EQUATION AND BUBBLE COLLAPSE

Considering a spherical bubble (see fig 1.3 [adopted from Brennen[1] [p.48]) with radius $R(t)$ in a relatively infinite domain of liquid whose Pressure and Temperature are P_∞ and T_∞ respectively. The pressure (P_∞) is assumed to be known, even regulated, and the temperature of the liquid (T_∞) is assumed to be homogenous and known [1] [p.48].

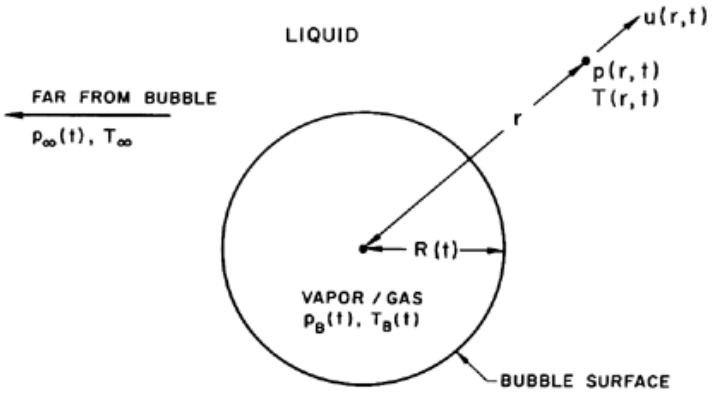

Fig.1.3 A spherical bubble in infinite liquid. [1]

Compressibility of the fluid is definitely important in the context of bubble collapse, but in this demonstration as described by Brennen[1] [p.49], it is assumed that the liquid has a constant density (ρ_L), and also the dynamic viscosity of the liquid is assumed to be constant.

The radius of the bubble, which is a function of time in bubble dynamics ($R(t)$), is very critical in this analysis, and the radial position will be denoted with r from the center of the bubble to the boundary. Within the liquid from the center of the bubble, the pressure ($P(r,t)$), the outward velocity ($u(r,t)$) and temperature ($T(r,t)$) are designated like that (see fig. 1.3).

Considering conservation of mass, the inverse-square law requires that the radially outward velocity $u(r,t)$, must be proportional to the square of the distance from the center of the bubble r (Brennen[1][p.49] and Grist[2]).

$$u(r,t) = \frac{F(t)}{r^2} \qquad (1.3)$$

Letting $F(t)$ be some function of time, where *F(t)* is related to *R(t)* by a kinematic boundary condition at the bubble surface. In the idealized case of zero mass transport across this interface, it is clear that *u(R,t)=dR/dt* and hence.

$$F(t) = R^2 \frac{dR}{dt} \tag{1.4}$$

If we consider a vapour bubble in the case of no mass conservation. Then we can assume that the rate of production of vapour must be equal or proportional to the rate of increase in size of the bubble.

$$\frac{dm_v}{dt} = \rho_v \frac{dV}{dt} = \rho_v \frac{d(\frac{4\pi R^3}{3})}{dt} = 4\pi\rho_v R^2 \frac{dR}{dt} \tag{1.5}$$

With V being the volume of the bubble, ρ_v is the vapour density and ρ_L is the density of the liquid. Therefore, the inward velocity of the liquid relative to the interphase is given by:

$$u(R,t) = \frac{dR}{dt} - \frac{\rho_v(T_B)}{\rho_L}\frac{dR}{dt} = \left[1 - \frac{\rho_v(T_B)}{\rho_L}\right]\frac{dR}{dt} \tag{1.6}$$

And

$$F(t) = \left[1 - \frac{\rho_v(T_B)}{\rho_L}\right] R^2 \frac{dR}{dt} \tag{1.7}$$

In many practical situations $\rho_v(T_B) \ll \rho_L$ and therefore the above equation is a good approximation. Considering momentum conservation and the bubbles boundary conditions the *Rayleigh-Plesset* equation is given by transforming time derivatives into space derivatives:

$$\frac{P_B(t) - P_\infty(t)}{\rho_L} = R\ddot{R} + \frac{3}{2}\dot{R}^2 + \frac{4v_L\dot{R}}{R} + \frac{2\gamma}{\rho_L R} \tag{1.8}$$

Given $P_\infty(t)$ this represents an equation that can be solved to find $R(t)$ provided$P_B(t)$ is known. In the absence of the surface tension and viscous terms, it was first derived and used by Rayleigh (1917).

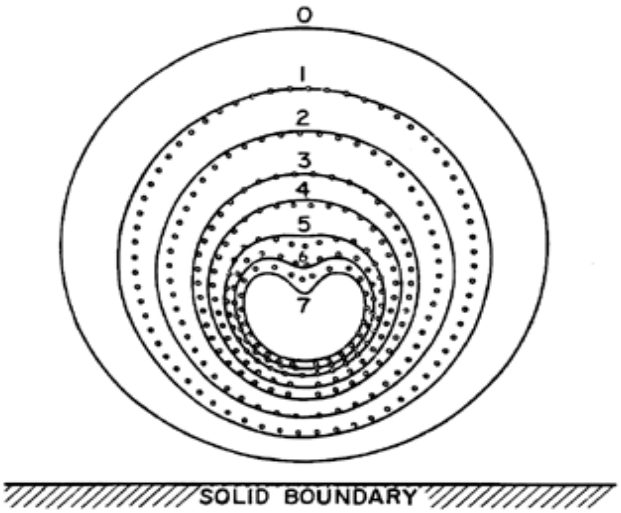

Fig.1.4 Collapse of a cavitation bubble close to a solid boundary in a quiescent liquid. Figure adapted from Plesset and Prosperetti (1977)

Plesset (1949) first applied the equation to the problem of traveling cavitation bubbles. With the derived Rayleigh-Plesset equation (eq.6) the flow dynamics closest to the spherical bubble in the liquid can be described. In this case the equation describes the interaction between the liquid and gas phase by bubble growth and disappearance.

Bubble collapse is particularly important because of the material damage and the noise caused by the high velocities, pressures and exaggerated temperatures that characterize the bubble collapse. Rayleigh-Plesset analysis assumes spherical bubbles. However, experimental studies show that bubbles that occur in cavitating flows do not remain spherical [1] [p.80].

Brennen [1][p.80] argued that the assumption of spherical bubbles is an assumption of the maximum case scenario, with maximum temperatures, pressures, noise and also worst case potential damage. Deviation from sphericity can diffuse the focus of the collapse and reduce the maximum pressures.

A dominant feature in the collapse of many vapour bubbles is the development of reentrant jet due to the asymmetry such as a nearby solid boundary. Such an asymmetry causes one side of the bubble to accelerate inward more than the other side and this forms a high speed reentrant microjet which

penetrates the bubble. Particularly interesting for cavitation damage is the fact that the presence of a solid wall result in a microjet directed towards the solid boundary.

In the experimental visualizations (carried out by Yang and Jaw[15]), the appearance of the counter jet during the bubble collapse is dependent on the distance from the center of the bubble to the solid boundary:

$$\gamma = \frac{d}{R_{max}} \tag{1.9}$$

Where R_{max} is the maximum radius of the bubble and d is the distance between the bubble center and the solid boundary. When γ is in the range of $1 < \gamma \approx 3$, a counter jet could be observed. However, no counter jet is generated under the condition of $\gamma > 3$.

The speed of the reenact jet U_j at the time it impacts the opposite surface of the bubble has been shown to be given by:

$$U_j = \xi(\Delta p/\rho_L)^{1/2} \tag{1.10}$$

where ξ is a constant and Δp is the difference between the remote pressure which would maintain the bubble at equilibrium at its maximum initial radius and the remote pressure present during collapse or responsible for the collapse. ρ_L represents the density of liquid. It is also important to emphasize that virtually all of the observations described above pertain to bubble collapse in an otherwise quiescent liquid. A cavity that grows and collapses in a flow as the one that will be investigated in the experiments that follow, is subject to other deformations and can significantly alter the damage potential and the noise of the collapse process.

1.4 CLOUD CAVITATION

Many experiments have been carried out on the visualization of unsteady cavitation close to a solid boundary. Particularly sheet cavitation happens close to a solid boundary and it has been characterized with periodic shedding of cavitation clouds. This happens with a sort of periodicity which can be evaluated to find a frequency of occurrence termed as shedding frequency. The periodicity is

accompanied with a reentrant motion, the growth of vortex cavity on the separated shear layer as well as shedding of large-scale cavitation bubbles in the form of a cloud as illustrated on figure 1.5. It is known that cloud cavitation, namely unsteady cloud cavitation, which has been characterized to produce some of the highest impacts at its collapse.

The mechanism of periodic shedding of cavitation clouds has been investigated by researchers such as Knapp [3] and Furness [4]. According to the investigation on hydrofoil cavitation by Watanabe [20], an unsteady cavitation of hydrofoil can be divided into two patterns due to the cavity length (ℓ). One is partial cavity instability and the other is transitional cavity instability. The latter instability which has heavy unsteadiness peculiar to hydrofoil cavitation while the former one which has characteristic frequency based on the cavity length can be directly related to the reentrant jet, (Franc, Michael [9]).

According to the previous studies [e.g., 6, 15. 20], the cloud cavitation is considered to be a self-oscillation phenomenon based on the re-entrant jet instability which is controlled by the thickness of separation zone and the adverse pressure gradient near the reattachment area of separation bubble. A study on a vibratory phenomenon was observed with a re-entrant motion as a feed-back mechanism in a convergent-divergent nozzle [7]. A cavitation cloud is observed to periodically shed downstream. The starting point of the periodical motion was an arrival of re-entrant motion at the leading part of attached cavity (see figure 1.5).

The most part in an attached cavity is occupied by vapor-liquid, two-phase fluid, namely bubbly mixture because the occurrence area of cloud cavitation is before the super-cavitation stage. Therefore, according to Sato and Watanabe research and experimental visualization [8], there were a few direct observations on the mechanism of cavity break-off though it was proposed that it can be caused by the collision or the contact of re-entrant jet with the surface of an attached cavity. Their study experimentally examined in detail about the turning process from the re-entrant motion to the shedding motion of cavitation clouds using a high-speed-video system.

Detached clouds will propagate downstream of the flow, the pressure starts to rise and when the pressure rises above the vapour pressure of the liquid collapse of the cloud happens. High spasms of energy during the collapse causes deformation and wear of the solid surface.

1.4.1 Re-entrant motion and cloud detachment

Using a high speed video visualization from a plane view, an observation of the shedding process was made by Sato and Watanabe [8] [p.3-4] which clearly show how cloud detachment takes place (see figure 1.5 (left)) and eventual cloud cavitation. The schematic view and the pictures taken by a high speed camera show the shedding process of cavitation clouds, especially the coalescence aspect of vortex cavitation clouds.

As demonstrated from the figure.1.5 - (1) first, an attached sheet of cavity separated from the nozzle throat or the solid surface grows downstream to a large scale. The attached cavity consists of bubbly mixture with reverse rolling flow at the closure part. The reverse fluid flows into the attached cavity to fill it as shown in figure 1.2 - (2) and as a result the bubbles tend to disappear inside the attached cavity. At this time a small scale break-off of cavity can, in some cases, occur as shown in figure 1.5 - (1)-b.

The reentrant jet was observed to go upstream as shown in the figure 1.5 - (2) and (3). For this study by Sato and Watanabe [8], pressure waves due to the bubble collapses was suggested to be the reason for the observed mechanism. The reentrant motion was estimated to advance upstream at a higher velocity than the propagation velocity of the attached cavity. When the re-entrant motion reaches the leading edge of attached cavity, and the bubble collapses there, a rushing out of fluid into main stream from the cavity inside occurs together with a rebounding motion of the bubble (see, figure1.5-(5)) and the formation of a small scale vortex cavity from the attached cavity occurs on the separated shear layer. However, the reentrant jet does not always reach the leading edge of the attached cavity. The detachment can happen at any point on the sheet cavity.

A vortex cavity formed by the fluid from the attached cavity grows through the coalescence with existing vortex cavities and is finally shed downstream as a large cavitation cloud (see, fig.1.5-(6)). It is not shown on fig.15 but the detached cloud shortly grows in size and then starts to collapse as it progresses downstream.

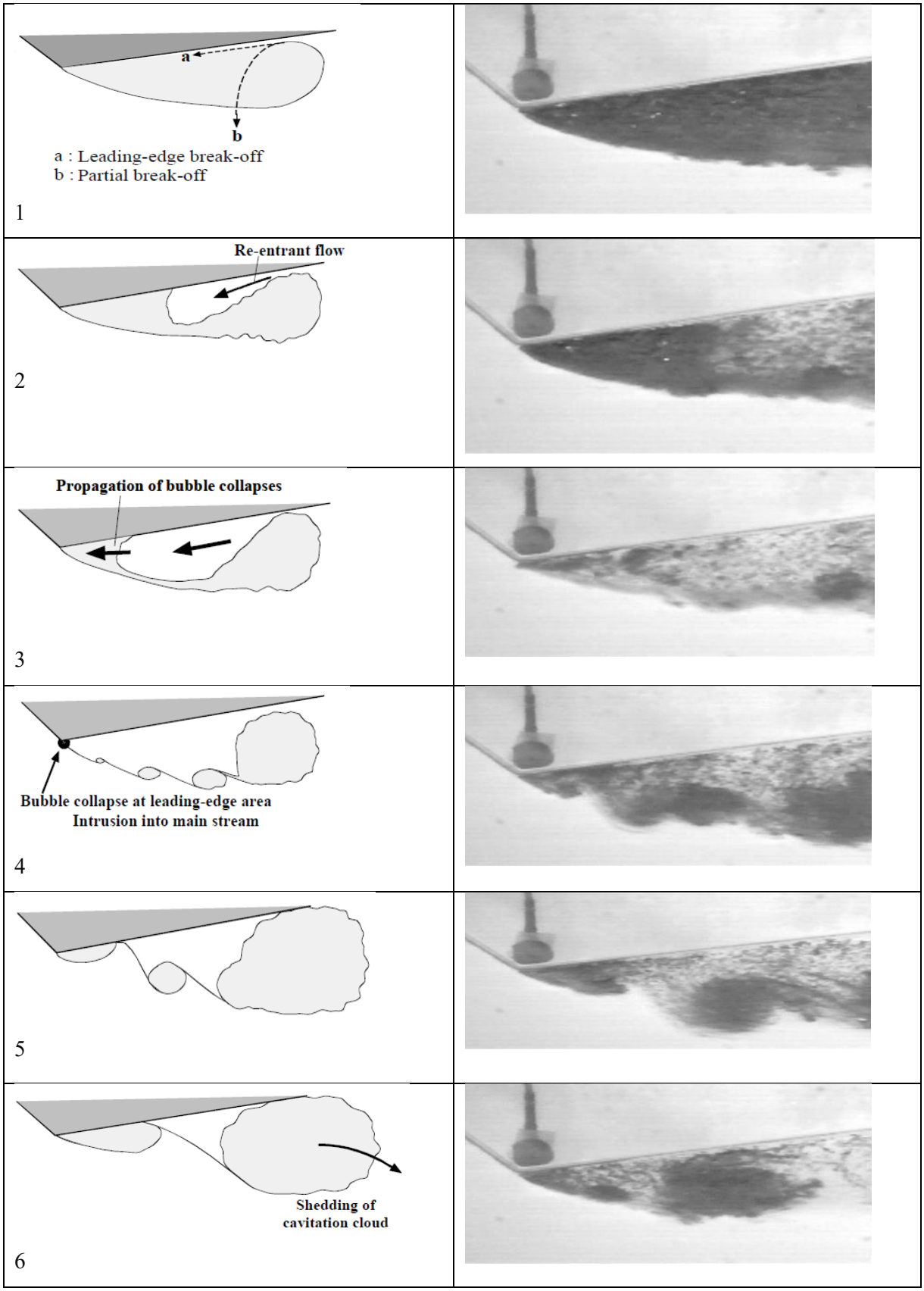

Fig.1.5 Schematic view on the process of re-entrant motion, cavity formation and cloud shedding (High-Speed Pictures Adopted from Sato, Watannabe 2003[21])

Visual observations of the cloud collapse have characterized it as a gradual division of the cloud into small groups of very fine bubbles, since the pressure rapidly rises due to deceleration of the cloud. With time the upstream part of the cloud again rapidly develops and the breakoff of the cloud again begins. In the experimental work that was carried out for this thesis, the effect of geometry and other hydrodynamic properties on this frequency was studied. Hitoshi and Yoshiaki [10] performed an experimental visualization of erosive cavitation clouds around a submerged water jet, and came to the observation and conclusion that the discharge intervals of the clouds scarcely depend on the nozzle geometry but it depends on the injection pressure. The length of the cloud is directly proportional to the jet velocity.

1.5 DIMENSIONLESS QUANTITIES

1.5.1 Cavitation Number

It is conventional in the analysis of cavitation, to characterize how close the pressure of the fluid is to the vapor pressure, and therefore the potential for cavitation to occur, by means of a pressure ratio parameter called the cavitation number. The most common adaptation of cavitation number is the one described in equation (11).

$$\sigma = \frac{P_\infty - P_v}{\rho . v_\infty^2 / 2} \qquad (1.11)$$

The pressure P_∞ is the pressure at the inlet of the test section, and P_v is the vapor pressure of the fluid. This is divided by the dynamic pressure - defined by the density ρ and the upstream velocity v_∞ [11] [p.35]. However, different literatures adopt different characterization of the cavitation number depending on the experimental setup and the practical complexities of measuring the different properties of the flow. In our experimental set up and evaluation we shall adopt the following cavitation number:

$$\sigma = \sqrt{\frac{P_{in} - P_{out}}{P_{in}}} \qquad (1.12)$$

Where P_{in} is the inlet rail pressure measured by a pressure sensor upstream of the channel. P_{out} is the outlet pressure. Any flow, cavitating or not, can be characterized by some value of σ. Refering to equation 1.12, increasing the cavitation number results in higher probability in cavitation occurrence or leads to an increase of the magnitude of the already present cavitation.

1.5.2 Reynolds Number

The Reynolds number is defined in terms of characteristic hydraulic diameter (h).

$$Re = \frac{v \cdot h}{\mu} \tag{1.13}$$

Where v is the velocity of the flow, and μ is the kinematic viscosity of the flow which is a function of the density and the temperature of the fluid.

1.5.3 Strouhal Number

Strouhal number is a dimensionless parameter used in the analysis of unsteady, oscillating flow conditions. It is normally defined in the following form:

$$St = \frac{f \cdot l}{v} \tag{1.14}$$

Where : f is the oscillation frequency of the sheet cavity. Or the shedding frequency.
l is the characteristic length.
v is the characteristic flow velocity.

On a publication by Vestnik [11], the different parameters that are normally used by different authors to define the Strouhal Number in cavitating dynamic flow has been discussed. In the past, different authors have chosen different definitions for the different characteristic quantities and therefore a vast span of different Strouhal Number can be calculated for each experiment. Some of the adopted definitions of the characteristic parameters are discussed below, which were adopted from Vestnik [11].

Characteristic shedding frequency.

Naturally this is quite consistent from all the authors and researchers. It is the cavity cloud separation frequency and can be determined by a number of ways. Most common being high speed visualization dynamic pressure measurements, time resolved PIV (Particle Image Velocimetry) [11], or pressure signal resolved over time. A relatively consistent number can be obtained from all the mentioned methods.

Characteristic length

Different authors have adopted different lengths when sheet and cloud cavitation is concerned.

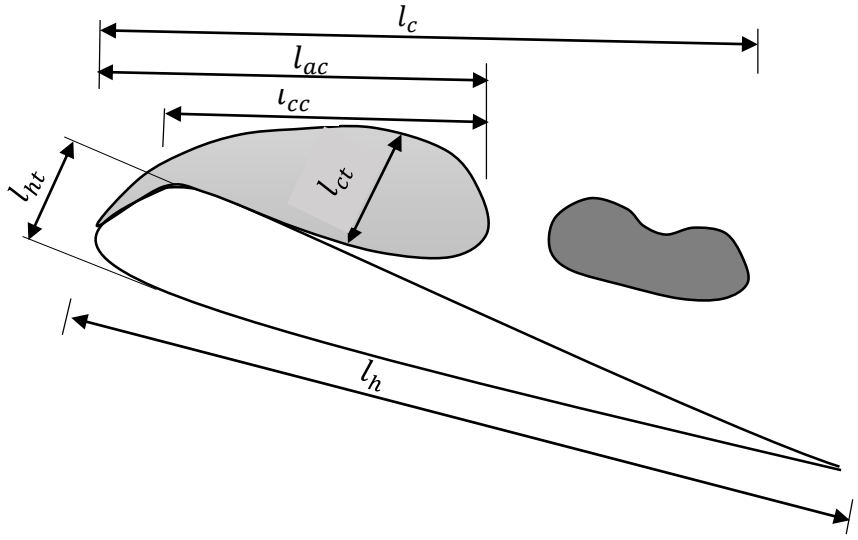

Fig.1.6 Interpretations for the characteristic length. Obtained from Matvez DULAR, Strojniški VESTNIK [11].

Figure 1.6 shows the different lengths that have been adopted by different authors before. l_{cc} is the mean length of the attached cloud. The cavity retracts after shedding and then advances downstream before the next shedding event. The mean length l_{cc} is thus calculated by finding the mean of the shortest cavity length during retraction and the length at detachment(l_{ac}). l_c is the mean length of the attached and detached cavity. l_h is the length of the hydrofoil. l_{ct} is the width or height of the attached cavity. l_{ac} -

this length can be used when situations just before the cavitation cloud separations are observed, the attached and the separated vapor structure can easily be distinguished and the appropriate length scale can be determined. This, the most accurate, approach (apart from measuring the mean length of the separated cloud) has been used by many authors: l_{ht} is the width of the hydrofoil [11].
It is very common to come across different authors adopting different characteristic lengths as shown above. When the flow is in a nozzle as this study will focus on, appropriate characteristic lengths can be l_c or l_{ac}. The length adopted in this study is l_{ac}. Also noteworthy, when channels and pipes are applied in investigations, some authors have in the past adopted the diameter or height of the channel as the characteristic length for evaluating the Strouhal number. In this study, length

Characteristic velocity

Similar to the characteristic length, the velocity also lacks unification and consistency among different authors. Some authors use the reentrant jet velocity at the closure of the attached cavity just before the cavitation cloud separates which is very complex to obtain while others use simpler definitions for the characteristic velocity.
The simplest to determine and most accurate, also most widely used, is the velocity upstream of the hydrofoil, or in the case of a nozzle, the velocity at the vena contrata. It is closely related to the cavitation and therefore it is appropriate for use in the study of cavitating flows.

1.6 THERMAL EFFECTS ON CAVITATION

Cavitation is sensitive to the temperature of the liquid. According to Brennen [12], cavitation growth is suppressed by temperature increases. At high temperatures the evaporation rate for the same bubble volume is higher than at lower temperatures.

According to Kim and Song [13], at higher liquid temperatures, the total heat needed for evaporation at the bubble interface and the temperature drop within the bubble (due to evaporation) are both larger. Inside the bubble, as the temperature decreases, the vapor pressure also decreases. Thus, the “effective” cavitation number is decreased, and the cavitation growth is delayed as the liquid temperature increases.

Probably due to the complexity of taking temperature measurements, most thermodynamic effects are usually estimated by rudimentary models. The most commonly used parameters in these approaches are the non-dimensional B-factor, which is a dimensionless temperature depression (Steppanoff 1961), and the dimensional parameters like ∑ (Brennen 1973), α (Kato 1984). Dular [14] performed a Study focused

on a single vapour bubble thermodynamic evolution. When the pressure drops the bubble begins to grow due to both the expansion of the gas contained inside the initial nucleus and the evaporation of the liquid. During the collapse the process is reversed – the main mechanisms are the condensation of vapor and the compression of the gasses. In both phenomena the magnitude of temperature variations in the thermal layer around the bubble depends strongly on the predominant process that drives the bubble size evolution. A thermal boundary layer develops in the liquid around the bubble. Its thickness is of the order of $\sqrt{\alpha_l \Delta t}$ (Franc *et al.* 1995), with α_l the thermal diffusivity in the liquid during the time Δt [14] [p.48].

The Fourier's law in the thermal layer around an isolated bubble can be written as follows:

$$\Delta Q \approx -\lambda_l \frac{\Delta T}{\sqrt{\alpha_l \Delta t}} 4\pi R^2 \Delta t = -\sqrt{\lambda_l \rho_l c_{pl}} \sqrt{\Delta t} 4\pi R^2 \Delta T \qquad (1.15)$$

Where ΔQ is the heat received by the bubble from the liquid, $\alpha_l = \frac{\lambda_l}{\rho_l c_{pl}}$, with λ_l as the thermal conductivity of the liquid, ρ_l is the density of the liquid, c_{pl} the heat capacity at constant pressure in the liquid.
Combining above equation and an energy balance equation as illustrated by Dular [14], an equation for Δt_r which is the characteristic time of heat transfer process at the bubble interface boundary can be derived:

$$\Delta t_r = \frac{(\rho_g c_{vg} R)^2}{9 \lambda_l \rho_l c_{pl}} \qquad (1.16)$$

The process can be considered adiabatic if the bubble life time is much shorter that the characteristic time of heat transfer Δt_r the bubble evolution is then mainly driven by expansion and compression of gases. In the opposite case, if there is enough time for the heat transfer to proceed until thermal equilibrium is reached ($\Delta t_r \ll \Delta t$), the process is closer to isothermal conditions, which means that evaporation and condensation of water and water vapour are the main driving mechanisms.

Assuming that the bubble size evolution is entirely due to vaporization or condensation, and we further simplify the analysis by neglecting the initial size of the nucleus and assuming that the growth velocity of the bubble is of the order of $R/\Delta t$ (see Brennen 1995) we get:

$$T_b - T_\infty = -\frac{R}{\sqrt{\alpha_l \Delta t}} \frac{\rho_V L}{\rho_l c_{pl}} \tag{1.17}$$

T_b is the temperature inside the bubble his equation provides an order of magnitude of what temperature differences should be expected in the liquid close to the bubble interface.

An equation adopted from Dular [14], shows the thermodynamic effect in terms of vapour pressure difference:

$$\Delta p_v = p_v(T_\infty) - p_v(T_b) \approx \frac{\rho_v L \Delta T}{T_\infty} \tag{1.18}$$

Which gives the decrease of the vapour pressure in the vicinity of the bubble due to latent heat flow (L). This equation demonstrates the idea suggested earlier in the literature that an increase in the temperature (T_∞) of the liquid could reduce the vapour pressure difference (Δp_v) and consequently, the rate of bubble growth.

An experimental study carried out by M. Dular [14], suggests that the main two mechanisms that drive the heat fluxes are the evaporation and condensation, while the other two – expansion and compression significantly contribute only in the very beginning and at the very end of the bubble life. The theory of thermal (Brennen 1973) delay was based on this observation.

1.7 CONCLUSION

From past research, some mentioned above, it can be perceived that the flow field of a cavitation bubbles and collapse is very complicated in addition to the difficulties of its visualization. The cavitation bubbles that are shed as a cloud collapse in a relatively short period of time. Even with an expensive high speed camera device used with framing rates more than 100 million frames per second, there are still many limitations for the measurement of the flow field characteristics of the bubbles collapse.

This study emphasizes the discussion, observation and description of the causes of the phenomenon of cavitation cloud and the formation, flow and collapse velocities of a cavitation bubbles.

Chapter two will concentrate on understanding the measurement and visualization technique. It will give an overview of the characteristics associated with the liquids to be used and the camera equipment. Some reference from research already made will be used to develop an understanding of the performance parameters.

Chapter 3 shall include a description of the visualization concepts, the procedures, the calibration work to be carried out on the analysis of the effects of cavitating flows. The evaluation and processing of the data collected from the experiments will discussed.

2 OPTICAL SETUP

2.1 HIGH-SPEED IMAGING

High-speed imaging in flow visualization is primarily aimed at obtaining precise information about the position and dimensions of the fluid flow at a series of instants in time, i.e. to resolve to the best possible extent the spatial and temporal scales. In this section, the concepts considered in setting the test rig will be described, the optical set up that will be used for the imagery of the high speed flow will also be explained. Initially it is important to estimate the average velocity or the highest expected velocities of the fluid to be investigated, and this will be crucial in determining the frames rates to use and therefore the specifications of the camera. Then the type of illumination techniques that can be applied will be discussed and a suitable one will be chosen. A general arrangement and layout of the equipment was then proposed and tested.

To figure out the range of frame rates that will be optimal for the imaging, it is important to have a good approximation of the relevant time scale of the high speed event. In some studies, the cyclic event of which the driving frequency is known, for example, if the shedding frequency is known or a close estimate can be established, the frame rate could be determined from this using the Nyquist Theorem [29] [p.8]. It establishes a sufficient condition for a sample rate that permits a discrete sequence of samples to capture all the information from a periodic event. According to the theorem, the sampling frequency, which in this case is the capturing rate of the camera, should be at least twice the highest frequency of the periodic event. Past experiments on visualization of cavitation shedding have the shedding frequency of various cavitating flows through venturi channels in the range of $0.5 - 7\ kHz$. The typical velocity of the of the flow will be used as a guide of the relevant time scale in this study. With reference to previous experiments and tests already carried out on our test bench, putting into consideration the highest recorded mass flow rate that the test bench can supply, and the geometry of the nozzles to be used in the cavitation investigation, the estimated highest velocity of the fluid to be expected is in the order of $210 ms^{-1}$. This is close to the expected maximum boundary condition, however, due to formation of the expected cavity structures at the surface of the microchannel the cross sectional area where the liquid flows will be reduced. This predicts a velocity slightly higher than the

one calculated above. But for the sake of determining the acquisition frame rate we shall consider the above velocity

According to Versluis [29], the optimum frame rate (f) can be estimated from:

$$f = \frac{N \cdot u}{l} \qquad (2.1)$$

Where N represents the required number of samples of images for every point the fluid is frozen by the high speed camera which we shall consider 3, which satisfies the Nynquist theorem. u is the typical velocity of the event, in this case the fluid flow maximum possible velocity will be used ($210\ ms^{-1}$), and l is the length scale, the length of the area of interest which we shall consider a length slightly more than the length of the channel's vena contrata. This consideration is made so that we can also observe the behavior of the cavity as it approaches the end of the channel and into the increased height opening (see figure 2.3). The vena contrata length is $750mm$ therefore l on equation 2.1 was considered to be $1\ mm$. Equation (2.1) shows the importance of high speed imaging in microfluidic application, where l is small and consequently f is large. The flow can therefore be visualized with a frame rate of the order of $600{,}000\ frames/s$. For our experiment we shall be using a *megapixel camera – Phantom v711* capable of taking up to *1,400,000 frames-per-second*, with *resolution of 1280 x 800* at *7,530 fps* and *300 ns digital exposure*. However, taking the images at such high frame rates will significantly reduce the capable resolution, and also the digital exposure time will be very low, therefore for this extreme case we have to consider a sufficiently high intensity illumination capable of working at such high speeds.

2.2 ILLUMINATION TECHNIQUE

Lighting is the next parameter to set, as it is one of the most critical aspects of any digital high-speed camera system, with a direct impact on the effectiveness and quality of the images. As one looks to utilize the full capabilities of camera – High speed Camera, using higher frame rates, in the order of magnitudes as stated above with the goal of visualizing high speed flows, it is increases the amount of light needed to properly expose the subject.

Technically, an increase in the frame rate and shutter speed of the camera reduces the amount of time that the light enters the camera and therefore for compensation, a higher light intensity is necessary. As a rule of thumb, every time you increase the camera's frame rate and therefore reducing the exposure

time of each frame, you're also increasing the intensity of light required to properly illuminate the sample. To achieve a good image quality, the camera quality, lens, the illumination techniques and focusing should be highly regarded.

Some types of light sources that are commonly used are:

- Conventional light sources
- Laser lights
- LEDs – Light Emitting Diodes
- Xenon lamps

Conventional light sources include spot-lights, quartz-iodine lights, tungsten lamps, mercury lights and electronic flash. These are some of the everyday light sources around us. Lasers is a device that generates an intense beam of coherent monochromatic light. LED lamps are electric lights that produce lights using light emitting diodes.

A very common problem associated with using the conventional sources of light is flickering. During the down cycle in the sinusoidal frequency of the current, the lamp filament is dim. This is not noticeable with our bare eyes but a high speed camera set at high frames per second will have a flickering effect in the image. If the frame rates to be used are sufficiently low, the problem can be solved by matching the frame rate with the frequency of the lights you are in. For high fluid high speed analysis, the frame rates required to capture comprehensive imagery are usually of very high orders and use of conventional AC lamps is not feasible. However, these lights can be used to take still images. The conventional lights essentially produce light by heating up of a tungsten filament and this leads to another problem of high temperatures, to be considered when choosing the source of light. Subjects imaged using high-speed cameras require large amounts of light to illuminate them. To leverage this amount of light from a conventional tungsten lamp, a relatively high amount of heat will need to be produced. Should your test subject be exposed to these high light levels for extended periods of time, the subject will get hot and its properties change [23]. For example, depending on the distance the lamp is from the test fluid during visualization of cavitation, the temperatures of the fluid, which are a crucial property, could be affected.

The commonly flicker-free sources of light used are *Lasers*, *LEDs* and DC lamps. All of these light sources, if well adjusted, are sufficiently constant to perform high speed visualization without any sort of flickering effect. In some situation they could actually be interchangeable, although other situations one could be more suitable than the other.

The table below compares some of the advantages and disadvantages of the two sources:

characteristic	**LED**	**Laser**	**Xenon Lamps**
Output power	Lower	High (order of MW)	Low (900W – 12KW)
Spectral width	Wide (40-190 nm)	Narrow (0.00001 – 10 nm)	Wide (1000 nm)
Numerical aperture	Large	Small	Very large
Cost	Less	More	Less
Ease of operation	Easier	More complex	Very easy
Safety	Safe	Very low	Safe

Table 2.1 Commonly used illumination sources for high speed flow visualization.

Due to the high speed of the flow in this experimental work, we will in principle resort to pulsed laser as the light source. This enables the sources of light to provide ample energy in terms of photometric light output per pulse, to be able to illuminate the sample for long enough and intensely enough to freeze the flow with a high-speed camera. The light source should be well controlled to sync with the camera and the pulse should be as short as several nanoseconds depending on the exposure time of the camera. This enables the pulsed mode of the laser to have higher power supplied because the high energy and intensity is supplied in a very short pulse duration.

Lasers are the most commonly used illumination sources due to some distinct characteristics that are useful for high speed flows visualization. Some of the reasons why lasers are mostly used are:

- Monochromatic and high-coherence light and changeable illumination optics
- High power and intensity with short pulses down to orders of 10ns.
- Ideal light source for schlieren and shadowgraphy applications.
- Versatility by varying pulse duration and repetition rate.

In general Lasers are more powerful and operate at faster speeds than LEDs and Xenon lamps, and they can also transmit light further with fewer errors. Pulsed laser source could be millions of times greater than LED and the other sources of light and a major advantage is that lasers accommodate more precise tailoring of the emitted wavelengths, pulse durations or laser powers to the particular system of interest. However, when using lasers for visualization, the coherence and the formation of speckles and optical fringes is a big drawback. Speckles refer to a random granular pattern which can be observed when a highly coherent light beam like laser light is used.

Aside from the dramatically reduced cost of procurement and considerably longer lifetime compared to lasers, an LED provides relatively incoherent light over a rather wider wavelength range (typ. ±10–30 nm) which alleviates many issues related to speckle artifacts found in laser-based illumination. If operated in pulsed mode, the luminosity signal of an LED is extremely stable, both in terms of intensity and spatial intensity distribution. On the other hand, the uncollated nature of the emitted light presents several challenges if the LED is to be used as alternative light source to lasers based in flow diagnostics. [24] [p.1].

According to the experimental analysis by Geoghegan1[6], which was illuminated by a custom built high-power-set LED system, the drawback with the LED illumination system in visualization of liquid flow experimental set up, is the rapid reduction of the light intensity as it propagates outwards and diverges. Therefore, it was necessary to use the LED light source very close to the flow to have sufficient light reach the camera. This of course is not a common problem with Laser lighting since the order of intensity is much higher than that of LED.

Xenon lamps are also commonly used in flow visualization with high speed cameras, they provide sufficient energy (up to 0.5 J pet pulse), however the pulse repetition frequency (PRF) for high-intensity flashes is limited, typically to 15 Hz or less. Increased flash rates are possible at the expense of decreased output energy.

High-power lasers offer sufficient light for back illuminating the target assemblies; however, laser speckle noise lowers the contrast in the image. Laser speckle noise also limits the effective resolution. A similar experimental setup was used by Mauger [30], to investigate the velocities in a cavitating 2D flow in a micro-channel nozzle. For illumination in the experimental visualization, an extremely short-pulse light was needed to optically freeze the flow. In addition, an incoherent light source was required to avoid speckle on images. In this work by Mauger [30], sufficient light source was generated by focusing the second harmonic of a *Nd:YAG* pulsed laser (wavelength λ = 532 nm and pulse duration $= 6\ ns$) on a fluorescent polymethyl-methacrylate (PMMA) sheet. This is one method that can be applied to reduce the coherence and consequently reduce the speckle noise associated with using a laser light source for imagery. In the active random medium (PMMA), light is scattered and the photons undergoes random 'walk' before leaving the medium, in this case polymethyl-methacrylate. By varying the density of the medium, the amount of scattering is varied and therefore the desired incoherence can be achieved. Many researches for example research by Hui Cao [31], have been carried out to describe ways of achieving incoherence in laser lighting and therefore a wide range of methods can be applied to reduce speckle noise in imagery. The fluorescent emission on Mauger's setup [30] was collimated and the remaining laser light was filtered using a band reject filter (Notch filter $\lambda_{notch} = 533 \pm 8\ nm$). The Nd: YAG dual head laser helped to produce time delayed light pulses. Each incoherent light pulse lasts

about twice the initial wavelength and (FWHM) and has a broad spectrum. This similar technique can be applied on our experimental setup, however, the intensity and energy supplied by the laser will be reduced due to interaction with the fluorescent medium. For average flow velocities ($10 - 80\ ms^{-1}$), images taken at $\approx 35{,}000fps$ would give a good analysis the cavitating flow and the shedding frequencies. A pulsed laser with high frequencies of $50kHz$ can be used and synchronized with the camera capture frequency to provide enough light intensity and at a sufficient pulse duration. Cavilux HF Laser has frequency ranging from $1kHz - 200kHz$, with a wavelength $\lambda = 810\ nm$, which can be sufficient for this range of velocities. Also considering the shedding frequency from past similar experimental work, and using the Nynquist sampling theorem, it puts this laser model at an ideal performance range for our study.

It is also common to use Xenon flash lamps at pulsed mode for similar experimental set ups. The pulse frequency of Xenon lamps doesn't match up to the high frequencies of pulsed laser; however, sufficient energy can be leveraged from the Xenon lamp and it is sufficient for relatively average velocity that require frame rates less than $100kfps$. Ezddin and Hutli [32] performed high speed experiments to make the aspects of cloud cavitation using an arc lamp as the illumination source. The set up consisted of Photron APX camera with a Corodin flash lamp system. The lamp was set to operate at a pulse duration of $0.5 - 11\ ms$ [32][p.2]. As expected, the photo resolution was the restriction factor for operating with the highest frame rates. At very high frame rates, about $50{,}000fps$, the resolution used was 256×64 at a shutter frequency of $1/250000\ s$, and the images were of sufficient quality to investigate the phenomena of cloud cavitation and calculate the shedding frequency and Strouhal Number. A similar shadowgraph set up was used by Biss, Settles [33] to capture the pattern of shock waves using a high speed camera and 1 kW Oriel Xenon arc Lamp, where the images were recorded at rates of $10000 - 75000\ fps$. This range of frame rates synchronized by a similar Xenon Lamp can be used to observe the cavitating high-speed flow on our set up.

The Xenon lamp has the major advantage of no speckle noise will be formed and therefore no complex setup required to make the light incoherent as required when using laser lighting. The laser has more intensity and higher frequency, if the camera has to operate at very high frame rates($> 150{,}000fps$).

With the estimated acquisition frame rate calculated from equation 2.1 which is dependent on the camera, the next consideration is the exposure time required to freeze the flow. The exposure time can be set by the camera or the light source.

Most importantly, so as to obtain a good temporal resolution and avoid blur and smear on the images, the exposure time of each frame should be maintained small enough to freeze the motion of the fluid flow. This temporal resolution is determined by the camera exposure time (τ_C) or by the illumination

time (τ_P). Evidently, the actual temporal resolution t will be the shorter of both durations, hence $\tau = min(\tau_c, \tau_P)$ [29][p.14]. If ϵ is defined as the displacement in pixels, of the object moving with velocity u during time τ then: $\epsilon = \tau \cdot u \cdot M/r_p$ where M is the magnification, and r_p is the pixel size. To obtain minimal motion blur the displacement in terms of pixels should be less or equal to one, $\epsilon \leq 1$. If the magnification and the velocity are pre-estimated, and the pixel size is known, motion blur can be avoided by using the following formula as suggested by Versluis [29]:

$$\tau \leq \frac{r_p}{M \cdot u} \qquad (2.2)$$

The formula above was used to determine the exposure time that we need to ensure as sufficient temporal resolution which was found to be $\approx 25\, ns$. This value can change depending on the magnification used and the effective velocity of the fluid. The camera used in this study is capable of a minimum exposure time of $\tau_C = 300\, ns$. Considering the expected velocity of the fluid, this exposure time is not sufficiently low to avoid blur, therefore we need to set and control the exposure time with setting the illumination time (τ_P). This can either be done by mechanical shutter or adopting a pulsed light source with pulse duration (τ_P) the same order as the required exposure time (τ).

A Cavilux HF laser was chosen to be used as the illumination source for this study. It is a pulsed diode laser light source, that can generate light power of hundreds of Watts. It generates monochromatic light with low coherence, which is ideal illumination for our purposes as it avoids speckle and chromatic aberrations. The laser can generate wavelengths of $810\, nm$ and the pulses produced can be adjusted to as low as $10\, ns$ pulse duration, which will ensure sufficiently low exposure time for freezing the images of the flow. The energy produced by the laser reduces with reduction as the pulse duration is reduced.

$\tau_{pulse\ duration}(\mu s)$	0.1	0.5	1.0	2.0	5.0	10
$E_{pulse\ energy}(mJ)$	0.05	0.25	0.5	1.0	2.5	5.0

Table 2.2. pulse energies for different pulse durations (P = 500W)

In this experimental work, the pulse duration adopted was between $20 - 30ns$, which was calculated from equation 2.2. The Cavilux HF laser has two operational modes, normal mode and high speed operation mode. At high speed mode the pulsing has a repetition rate up to 2MHz. This satisfies the estimated acquisition frame rate of the camera. The energy from the laser was also sufficient for the illumination purposes needed in this experimental work.

2.3 SHADOWGRAPH-LIKE VISUALIZATION SET UP

This experimental study will be applying a shadowgraph-like visualization technique where the flow will be back lit, and the shadow-like images will be captured by the high-speed camera. The physical layout of the high-speed camera, the micro-channel and the flow, and the illumination will be parallel. Shadowgraphy is the most common set up used for visualization of multiple phase flows and spray mechanisms because it provides a comprehensive image of the different phases and the density gradient in the flow. Figure 2.1 shows the schematic of the technique used in shadowgraphy.

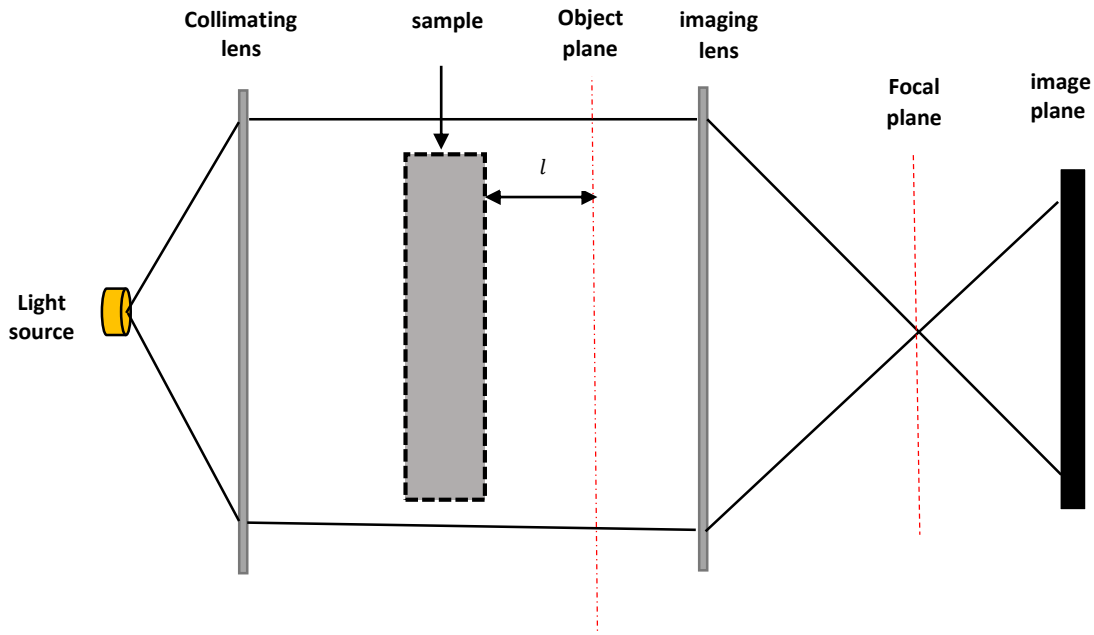

Fig. 2.1 Schematic of the standard shadowgraph technique

This method of flow visualization is dependent on the sensitivity of light intensity to difference in the densities (refractive index gradients) in a two phase flow. The different phases in the flow, will have a different refractive index and therefore cast a shadow with varying light intensities which makes the two phases visually distinguishable. The imaging lens is focused on the object plane, which is at a specific displacement (l) with respect to the sample of interest, usually fluid flow. The intensity of the shadow effect, or the sensitivity of the shadowgraph, increases with the distance l. On the other hand, the flow picture will be more out of focus with an increase in l, so that a compromise between optical sensitivity and image quality has to be found [34][p.3].

For this experimental set up, we shall use an arrangement much like the one used for shadowgraph technique, where the light source and the camera are placed on the opposite sides of the flow channel. The difference from the typical shadowgraph method is that the camera is focused directly onto the specimen in order to observe cavitation phenomena.

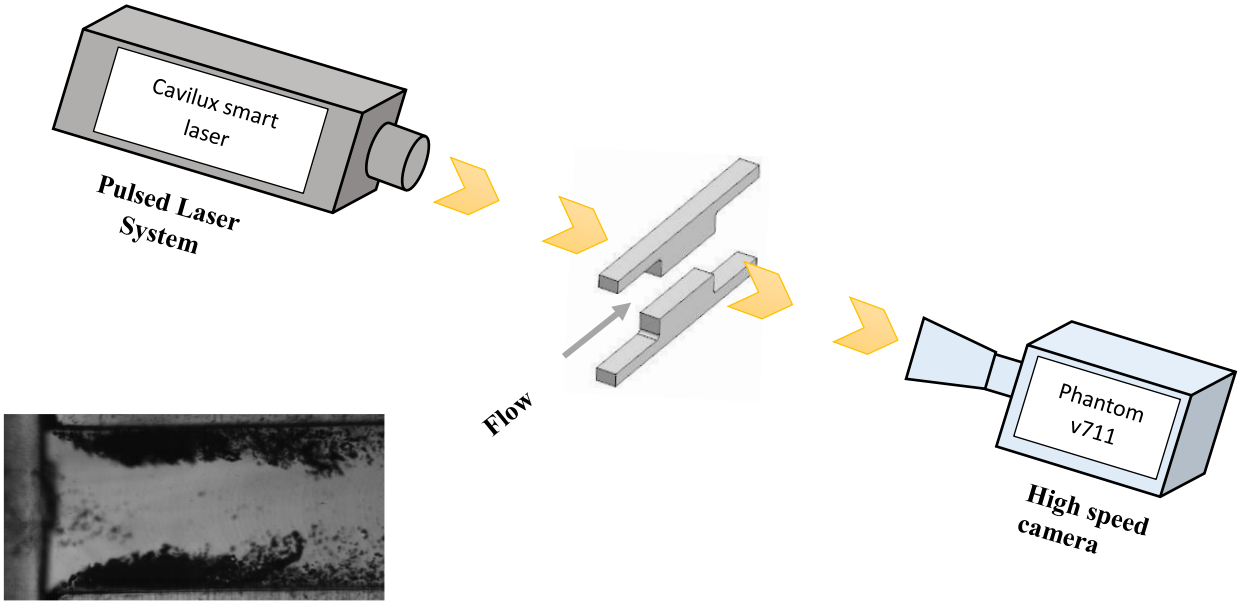

Fig 2.2 schematic of shadowgraph-like optical arrangement applied in this experimental study, high speed image through shadowgraph-like technique of visualization of a cavitating flow in a micro-channel: image obtained from: D. Funfschilling et al [35].

The working principle for this visualization, is that most of the rays crossing the interface of liquid and vapor are refracted with a greater angle than the collection angle. As a consequence, bubbles and vapour cavities will be expected to appear dark in the image. The liquid phase will appear brighter, since there is no ray deviation.

3 EXPERIMENTAL RIG AND 2D CHANNELS

Three geometries were applied in this study. The flow will be investigated in a 2D (in all intent and purposes) orifice, which is a simplified imitation of a nozzle (micro-channel) as shown on fig.2.3. The micro-channel will be continuously supplied with fuel, at predetermined upstream inlet flowrates and pressures. Referring to the channels described in fig 2.3, 2.4 and 2.5, the fuel flows from left to right though the constriction. The channels are mounted between two durable sapphire glass windows.
The camera will be focused at the vena contrata as this is where the cavitation is expected to initiate.

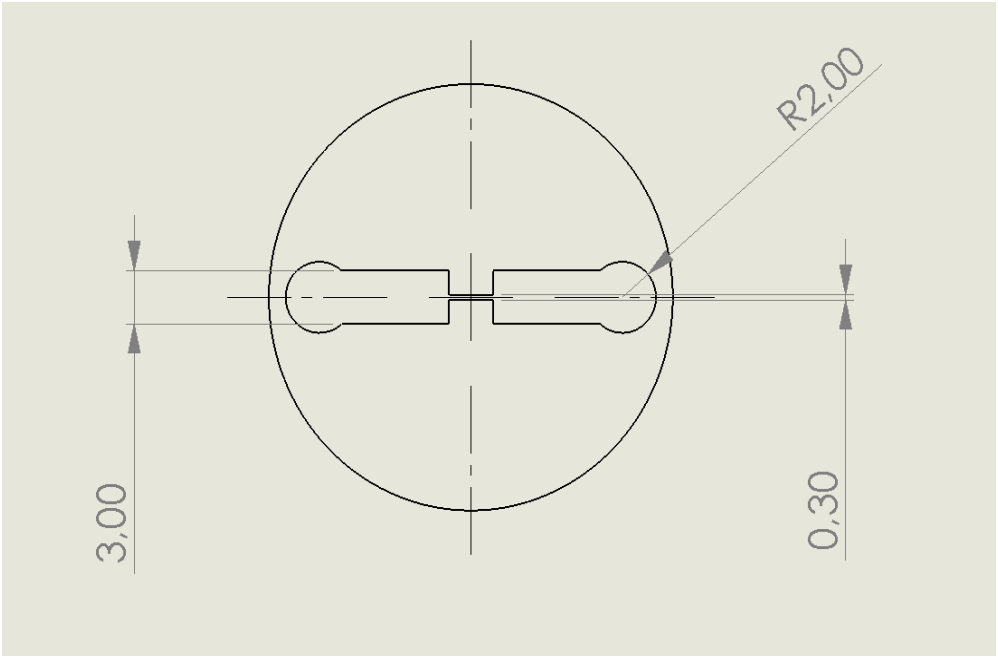

Figure 3.1. Channel 1. The vena contrata has a height(h) of 0.3mm. the thickness is 0.3mm which is consistent for all the channels uses in this study. Length of the constricted part is 0.75mm.

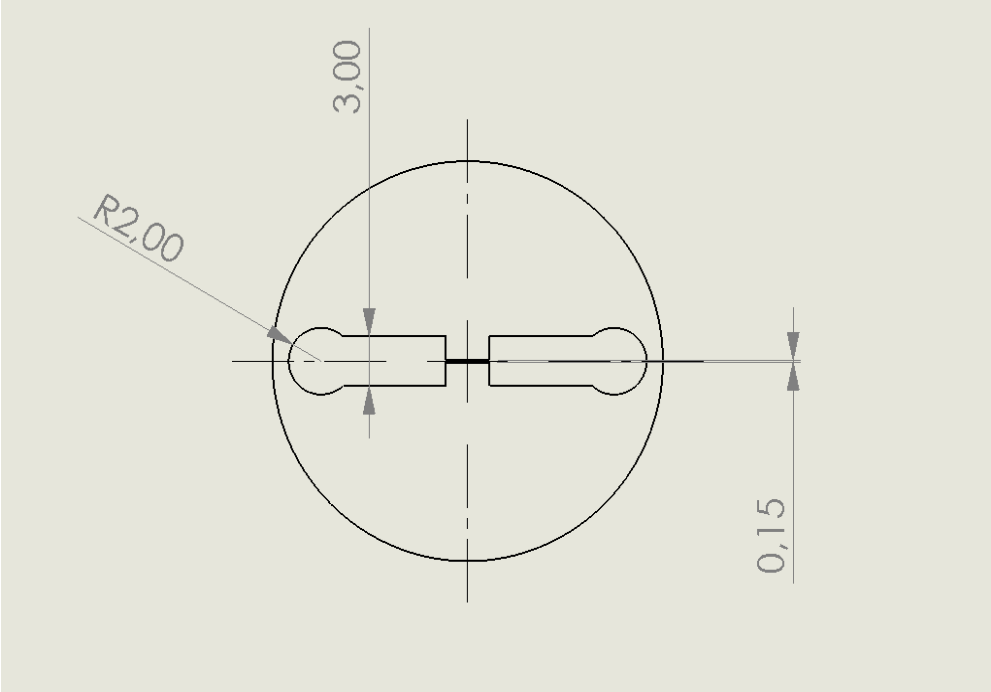

Figure 3.2. Channel 2. the height (h) of the vena contrata is 0.15mm. depth of 0.3mm. Length of the constriction is 0.75mm

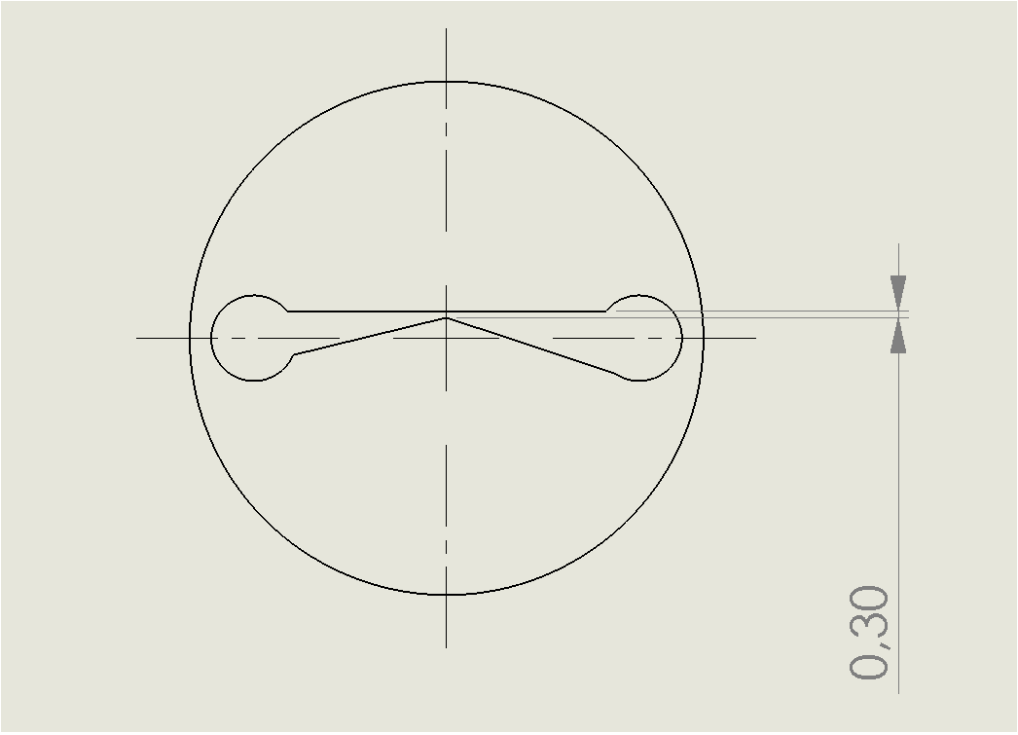

Figure 3.3. Channel 3. Converging diverging micro channel with vena contrata height (h) of 0.3mm. the depth is 0.3mm. The angle of convergence is 8.9º and the divergence angle is 6.5º.

Fig 3.1 shows the standard channel used in most of the tests done in this work. The constriction has a height (h) of 0.3 mm. As shown on the diagram the fuel is pumped from left to right in all the three channels. The circular opening at on the left in all the three channels has a diameter of 4mm. This is the inlet opening. The fuel then goes through the 3mm channel opening before entering the constriction. The length of the narrowed section is 0.75 mm. This is our region of interest since cavitation is expected to initiate there.

Figure 3.2 is a drawing of the second channel with the same dimensional values but the vena contrata is 0.15 mm. The thickness of all the channels is o.3mm. Channel 3 is represented with figure 3.3. It is the simplified diverging converging throttle. With a leading edge angle of 8.9º and a diverging angle of 6.5º.

All the channel plates were made of steel. Previous tests had concluded that steel had minimum to no erosion if the material of the plates was steel. Of course this was the desired condition for the test plate since any sort of erosion would change the geometry of the throttle, and the cavitation behavior.

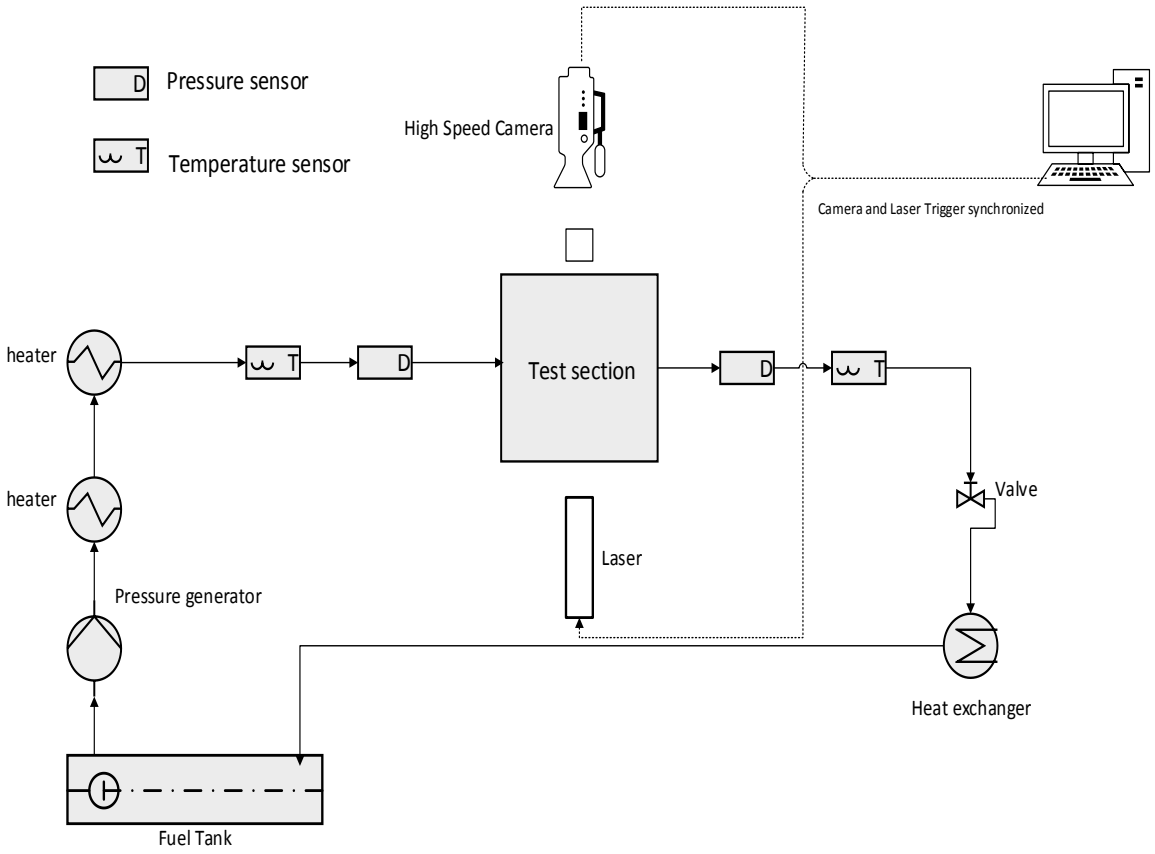

Figure 3.4. Schematic of the experimental rig

Figure 3.4 represents the schematic of the setup. Two heat exchangers upstream are used to heat the fuel to temperatures in the range of 10 ºC – 140 ºC. Downstream the test section another heat exchanger is mounted to cool the fuel. The pressure generator consisting of three pumps will be used to set the rail pressure. Also another heat exchanger is mounted downstream to cool the fuel. A pressure strobe sensor and a temperature sensor are mounted before and after the test section as shown on the schematic above. The pressure range for this experimental study is 0 to 300 bar with regard to the glass windows which risks breakage at higher pressures. The supplied flow rate range is from 0 to 15.9 g/s. Experiments were done with calibration fluid ISO 4113 and dodecane as the test fuels.

The variable boundary conditions in this experimental study will therefore be investigation of how the flow of different fuel-like liquids behave under variable parameters i.e varying the pressures drops, temperatures, flowrates and with different micro-channel geometries.

4 EXPERIMENTAL RESULTS AND EVALUATION TECHNIQUE

In this chapter the measurement approach and the evaluation method will be presented and illustrated. The images captured will be used to investigate the shedding process, cavity propagation and the collapse. The results after evaluation will then be presented and explained in the next section.

A complete cavity shedding event is shown in the sequence of images below (see figure 4.1 and 4.2). A sheet cavity can be seen at the initial stage. The sheet cavity is formed at the inlet edges of the throttle. The explanation for this is the sudden and sharp drop in the pressure of the fluid as it enters the throttle. If the pressure drops below the vapour pressure of the fuel, then a vapour cavity is formed. The cavity structure forms both on the lower and the upper surface of the channel. The shedding process and the collapse of the cavity as it propagates downstream the throttle can be observed in the high speed videos. After the sharp pressure drop at the leading edges of the throttle, pressure recovery happens gradually downstream the throttle and therefore gradual process of collapse of the cavity is observed.

The cavitation behavior is a function of the geometry. In the following section a description of the cavitation behavior as observed in a parallel throttle and a converging diverging throttle is discussed. The geometry of the three channels used in this study has already been described in the previous chapter (Chapter 3).

The high speed videos taken enabled the visualization and identification of different cavitation regimes which are non-cavitating regime, partial cavitation regime with periodic shedding, and the super-cavitation regime where the periodicity is noisy.

For the parallel channels 1 and 2, at low inlet pressure and low cavitation number ($\sigma < 0{,}71$), sheet cavitation and shedding could not be detected. For these channels (1 and 2) detectable cavities and subsequent shedding was observed at cavitation number $(\sigma) \approx 0{,}71$. However, in the converging diverging channel (channel 3) cavitation was observed at a much lower cavitation number of $(\sigma) \approx 0.61$. This was one of the distinct behaviors of the cavitation structures observed with change in geometry.

Increasing the cavitation number developed the non cavitating flow to partial cavitating flow. Periodic shedding is observed and a shedding frequency can be established. It will be discussed how changing the cavitation number within this regime has significant influence on the length of the cavity and the frequency of the cavity.

Further increasing the inlet pressure and the pressure difference between inlet and back pressure advanced the cavity to supercavitation or fully developed jet cavitation. The distinct differences between the regimes shall be discussed.

In this study the focus was on the partial cavitation regime, therefore the experiments' operating points were kept at a certain range of cavitation number which delimits the flow to this regime. This was because cloud cavitation has been known to be the aggressive in terms of the erosion associated with it due to the periodic collapse of the shed cavity.

As described in the research by Barber [35], the periodic shedding observed in this cavitation regime is a form of instability, which is driven by the re-entrant motion of the cavitation jet.

Figures 4.1 and 4.2 are a sequence of high speed images taken showing the process of shedding event. In all images the flow is from left to right and time is passing from top to bottom. The images on Figure 4.1 for the parallel channel were taken at a frame rate of 800,000 frames per second and therefore the time interval between each image is $1.25 \times 10^{-6}\ s$. The ones for the converging diverging throttle on figure 4.2 are recorded at a rate of 500,000 frames per second, with an inter frame time of $2 \times 10^{-6}\ s$.

Figure 4.1 of the parallel channel with height (h) of 0.3 mm, the detachment of the cloud is observed, it propagates downstream and collapses gradually. Converging diverging throttle depicts the growing, shrinking and shedding motion of the cavitating jet. The attached cavity length is observed to increase to its maximum length and then a part of the cavity detaches and propagates downstream to its implosion. The reentrant jet motion can also be observed as noted on the images. It is already known and keenly described on the previous work by Barber [35] that the reentrant motion is the driving force of the periodic shedding. The driving force for the reentrant jet motion has been suggested and demonstrated through high speed experimental observation on the work by Barber [35] to be the collapse of the cloud.

Therefore, it is suggested that the collapse of the previous shed cavity downstream causes a travelling pressure wave which creates an instability upon interaction the attached sheet cavity. This initiates the reentrant motion which in turn leads to a detachment. Fig. shows at time $t_0 + \Delta t$ the initial stage of the reentrant jet motion. The jet can be traced to move upstream creating a sort of detachment of the attached cavity from the surface of the channel.

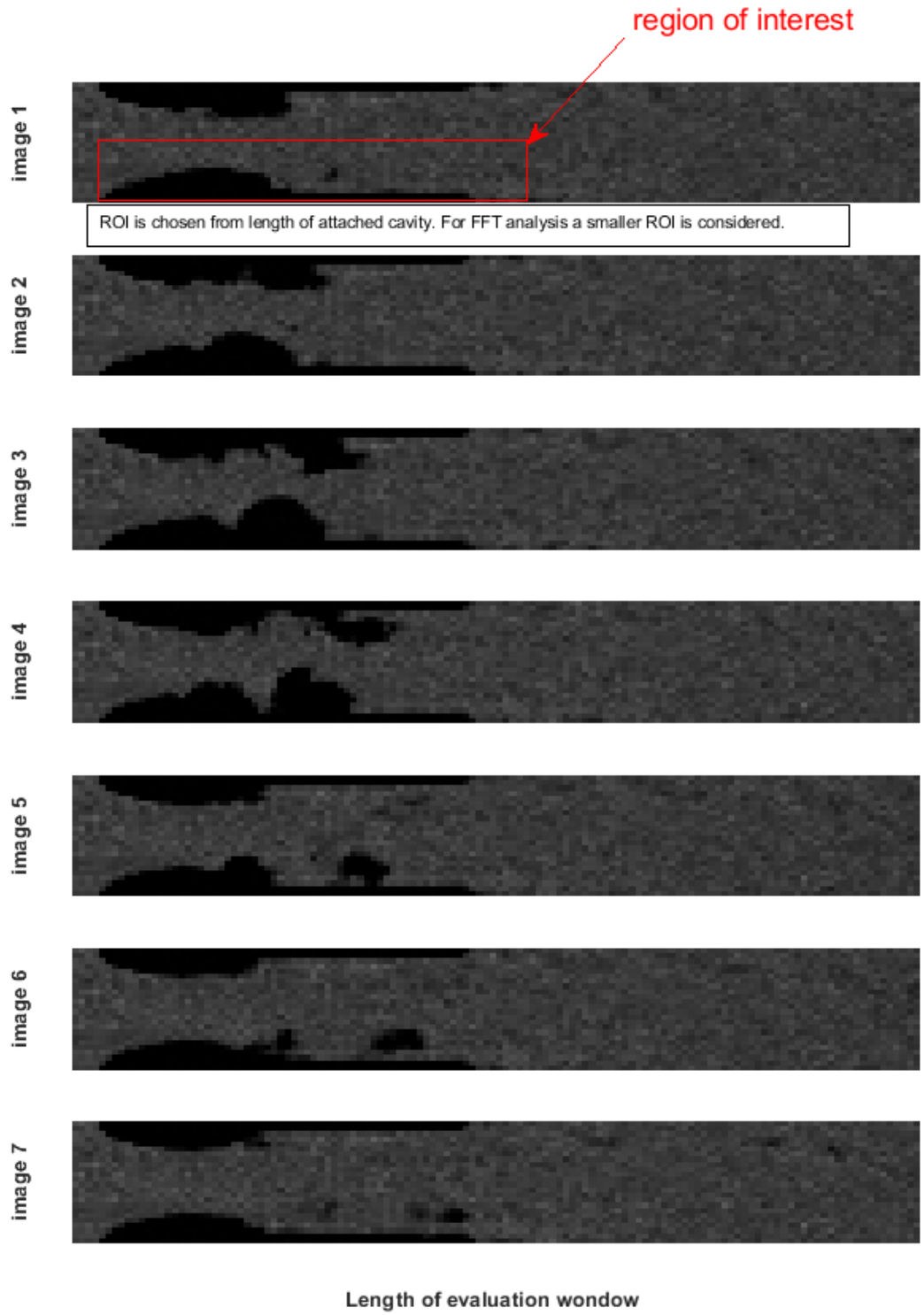

Figure 4.1. Image 1 to image 7 show the gradual process of one event of cavity detachment and collapse in a parallel throttle.

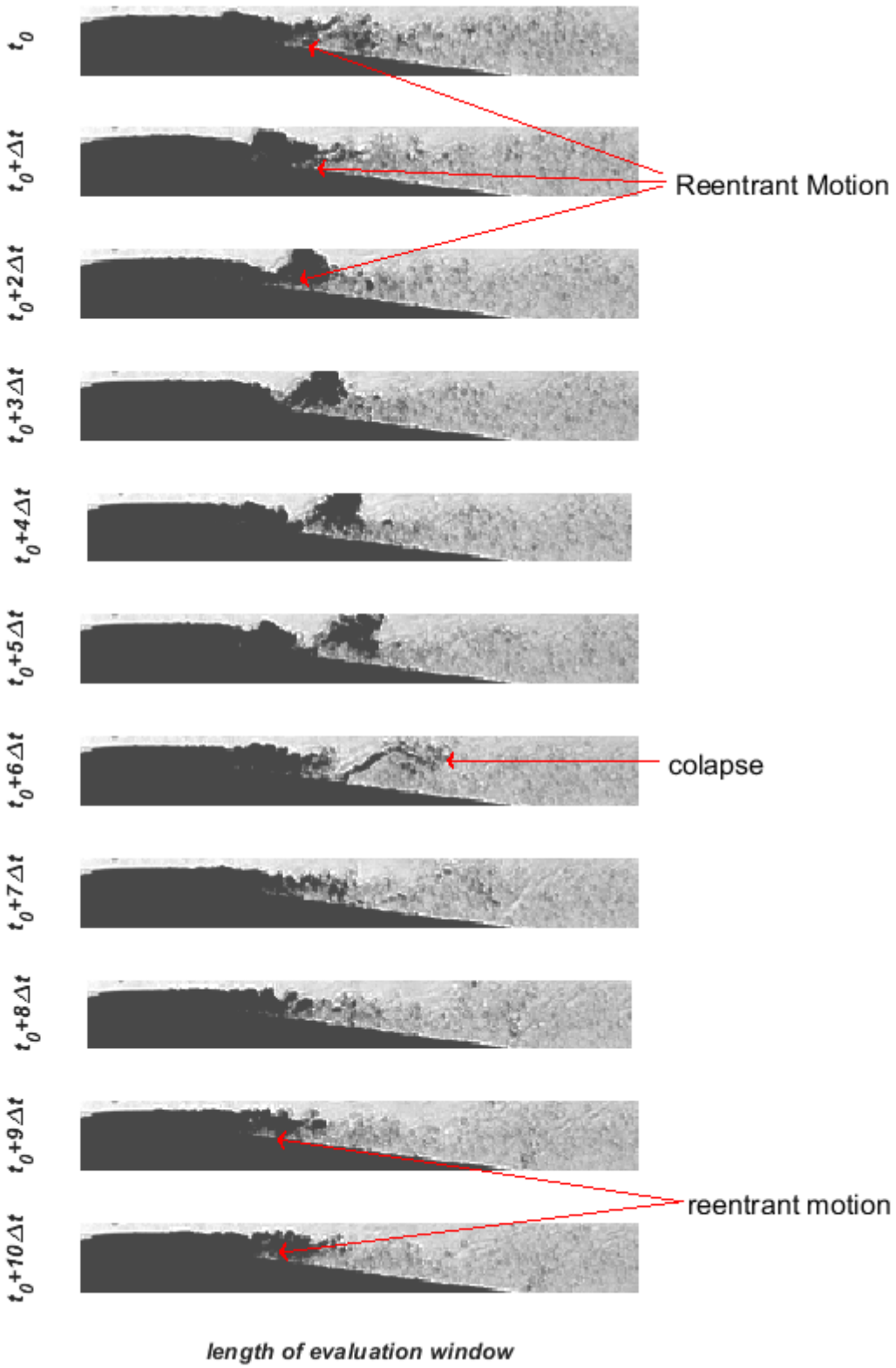

Figure 4.2 Set of images are a back to back set of images representing one event of detachment in a converging diverging throttle.

The progressive shedding of the cavity and propagation downstream is then observed from instance $t_0 + 2\Delta t$ to $t_0 + 6\Delta t$ where rapid collapse begins. At this instance the attached sheet cavity is attached to the surface. Thus in support of the observations and hypothesis explained by Barber [35], the detached cavity collapse seems to trigger the reentrant motion which again starts to reappear at time $t_0 + 7\Delta t$. This appears as a deformation on the underside of the cavity surface as pointed out at time $t_0 + 9\Delta t$ and time $t_0 + 10\Delta t$. This marks the initial stage of the subsequent shedding.
Also noteworthy, the size of the detached cloud increases in size after detachment then as it propagates downstream it starts to collapse.

4.1 IMAGE ANALYSIS APPROACH

This method is based on image processing of a sequence of images on image processing tool box. Image analysis method was used to get a close estimate of the velocity and the frequency of shedding and also get information on the periodic length change of the attached cavity.

To demonstrate the propagation velocity of the cavity and the behavior of the cavitation in general, an area of interest starting from the initial point of the attached cavity is selected. The area of interest has pixel dimension of $m \times n$. In this demonstration, the operating points described in the images above was used. The gray scale is averaged vertically for each column of pixels in the selected ROI. This is done for each time interval (each image) over a certain time duration (number of images evaluated) which in this example consists of 800 images and the acquisition frame fate used was 800,000 fps for the parallel channel and 500,000 fps for the converging diverging channel. The inter frame time is $\Delta t = 1.25 \times 10^{-6} s$ and $\Delta t = 2 \times 10^{-6} s$ respectively.

As seen on figure 4.1 and figure 4.2, the pixels with cavity are dark and those without are bright. Therefore, when the gray intensity of Region of Interest is vertically (column-wise) averaged, the $1 \times n$ matrix obtained can trace the position of the cavity. The parts with low average gray intensity (dark) represent the pixels occupied by the cavity and vice versa. When this plot is compared with the subsequent plots over time, the cavity propagation can be traced and the velocity can be estimated by tracing the position of the cavity over the x direction and using the inter fame time Δt to get the time scale.

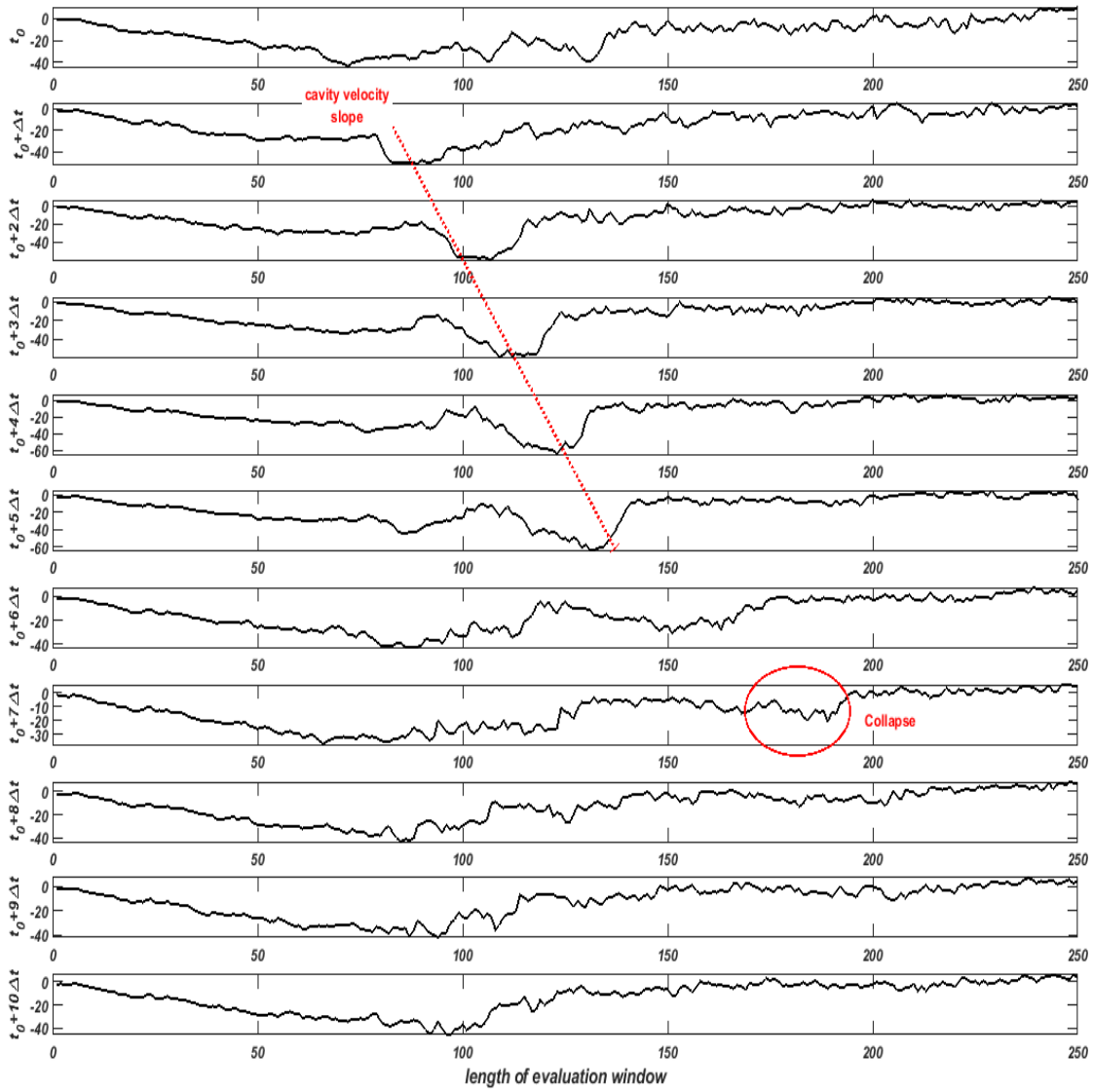

Figure 4.3. The vertically averaged values for one cavity shedding event represented on (Figure 4.2).

The figure above is the plot of the vertically averaged gray intensity for the cavity shedding event imaged on figure 4.2 for the converging diverging throttle. The slope line shown in the figure gives a good estimate of the propagation velocity of the cavity. The cavity from the instance $t_0 + \Delta t$ to $t_0 + 6\Delta t$ covers a distance of $d = 0.392\, mm$. The time interval is $5\Delta t = 1^{-5}\, s$.

The cavity velocity is therefore, $\approx 40.5\, m/s$. The velocity of the free fluid flow at the vena contrata in this case is calculated to be $90\, m/s$. It can therefore be asserted that the structures of the cloud cavitation propagate at a velocity smaller than the mean free velocity of the fuel.

To further understand the cavity global behavior, a larger time interval (more images) was considered. A $m \times n$ matrix is derived where m represents the number of images and n is the column gray intensity for each image.

To demonstrate this, the operating points considered above will be used for the converging diverging throttle and the parallel throttle. First step, the channel was subtracted from the images to isolate only the cavity dynamics. In this illustration, 800 images were used in both cases. This is $1.6^{-3}\ s$ time interval for the converging diverging throttle and $1^{-6}\ s$ for the parallel throttle.

For the converging diverging channel ROI is the entire image which has a resolution of 256×32. 256 pixels horizontally and 32 pixels vertically. The column-wise averaged gray intensity for an interval of $1.6^{-3}\ s$ will thus procure a 800×256 matrix representing the averaged gray intensity over the whole interval.

For the parallel channel, as seen on figure 3.1, the cavity length and propagation distance is much shorter. A length of 50 pixels was considered. The matrix from the column-wise averaged intensity has dimensions 800×50. The matrices can be interpreted as an image which shows the dynamics of the cavity over time.

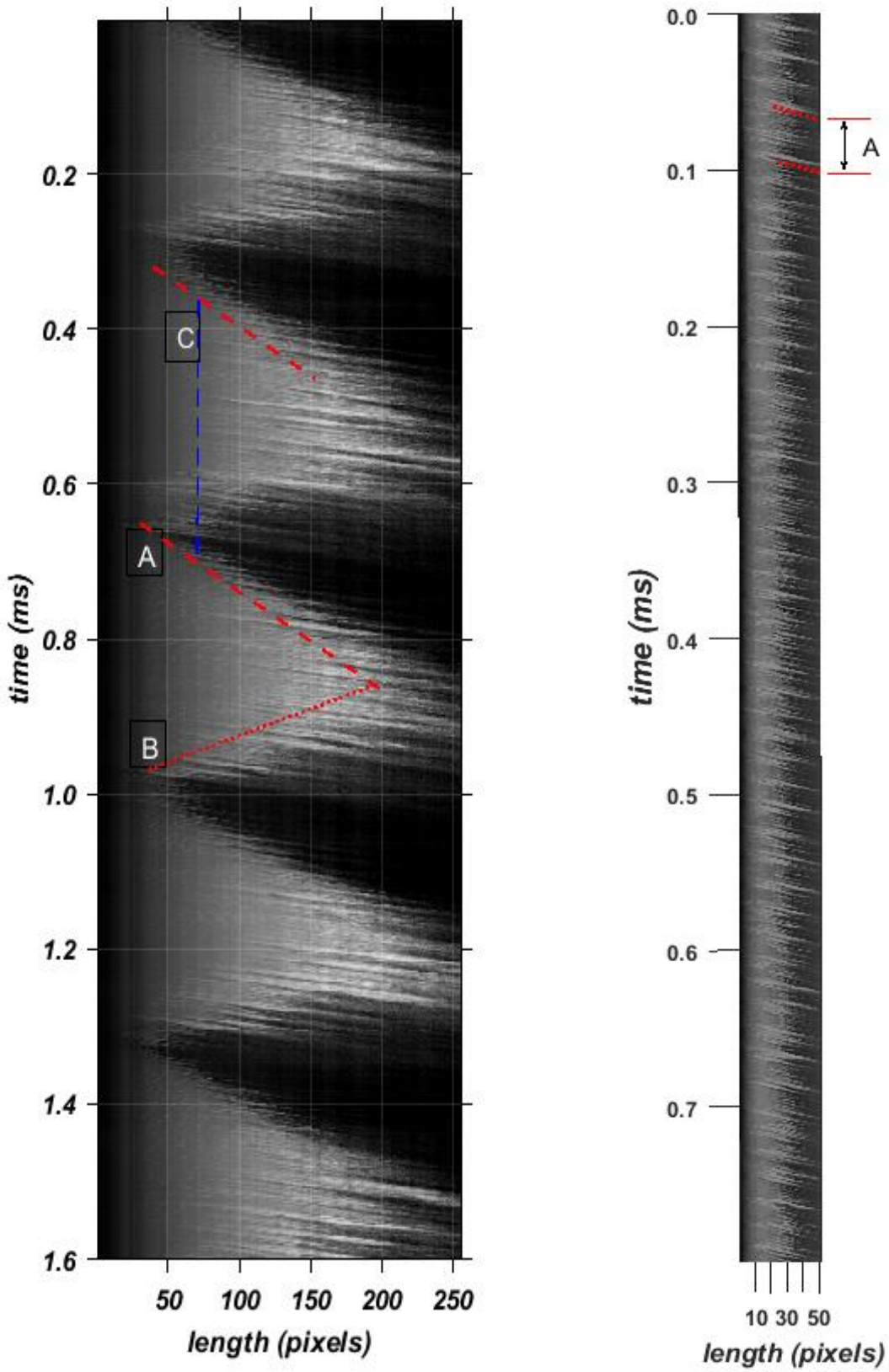

Figure 4.4. Images of averaged gray scale for a converging diverging channel (left) and parallel channel (right).

Figure 4.4 represents the images plotted from the matrices formed by the column average intensity for 800 images of the two channels. The first image (right) represents the parallel throttle at P_{inlet} = 50 bar and cavitation number 0.78, recorded at frame rate of 800,000 frames/s. The image on the left is the plot of the vertical averaged gray intensity of the converging diverging throttle at P_{inlet} = 50 bar, images captured at a frame rate of 500,000 frames/s.

The images of cavitation on the converging diverging throttle show the progressive growth and retraction of the length of the attached cavity. The diagonal slope line A represents the average length growth velocity of the cavity. For this case illustration it was calculated to be $9\ m/s$. Slope line B represents the retraction velocity of the attached cavity. The retraction velocity is estimated about $15\ m/s$. The image for the converging diverging channels shows distinct periodicity in the change in length. The vertical line C, represents the period (τ) of two length growth events. The frequency can be evaluated ($1/\tau$) which was found to be $3050\ Hz$. This frequency will be confirmed in the next section. Cavity detachment (shedding) happens at a much higher frequency. During each change in length cycle, periodic cavity detachment happens.

Referring to figure 4.4 (converging diverging) the shedding is represented by the multiple lines observed on each cycle of length change. The attached cavity periodic change in length was observed to be very distinct on the converging diverging throttle. However, as the image of the parallel throttle delineates, there change in length of the attached cavity is not very distinct relative to the shedding process. The shedding periodicity is well observed also in the case of the parallel throttle. This gives the possibility to get a close estimate of the shedding frequency by using the interval time between two shedding cycles. The line [A] on the figure 4.4 represents a period between two cycles. The frequency in this illustration case is calculated to $\approx 70\ kHz$. This frequency was also confirmed with the FFT method demonstrated in the following section.

This method of analysis provides insight on the internal structural behavior of the cavity. It provided a good estimate of the time scales and velocities of the shedding and the length oscillation events. However, it is limited by the number of images that can be used to still have an image that can be evaluated clearly. To evaluate a larger time interval and a global understanding of the different frequencies involved, a Fast Fourier transform was taken for the average gray intensity signal over time.

4.2 FREQUENCY EVALUATION APPROACH

The FFT approach was adopted mainly because of its accuracy and precision when analyzing frequencies using larger time signal. As will be demonstrated in this approach, the number of images used for one operating point frequency evaluation is larger ($\approx 60{,}000\ images$) compared to the image analysis approach which has a limitation in this sense. In this approach, sufficiently small rectangular areas of interest of $m \times n$ pixels were chosen as shown on the images above (see figure 3.5). The region in this case, differing from the one used in the previous evaluation technique, was chosen to be sufficiently small to ensure that only one detached cavity passes through the ROI at any given time. It is important to note that the precision and accuracy of this evaluation technique was dependent on the choice of the region of interest. This is because due to superposition of cavity shedding and change in length gave rise to different frequencies for the different events. Having multiple regions of interest (1,2,3,4) as shown on the image on figure 4.5 made it possible to compare the different frequencies at different lengths. Cavities go through more than one region of interest and a comparison of the frequencies increased the precision of the data. Gray scale is either low when there is a cavity or high when there is no cavity.

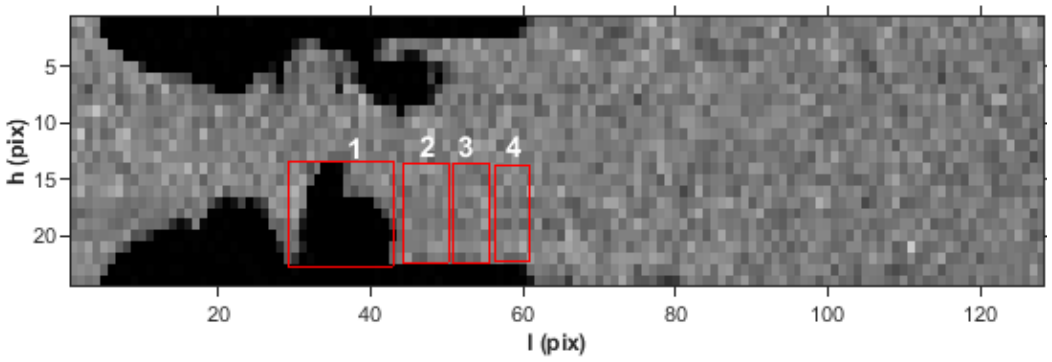

Figure 4.5. Definition of the ROI for frequency evaluation

For each evaluation (each operating point), the multiple regions of interest were evaluated and the FFT frequencies compared. The level of concurrence of the FFT frequencies found at the different regions of interest further helped to understand the different dynamics of the cavitation. To understand this, one can imagine that some cavities will collapse before they reach the ROI on the further right (figure 3.5, region 4), while some cavities travel longer before they collapse. Adopting the multiple regions of interest provided more insight on the frequency of the cavities collapsing further downstream the channel and those that collapse soon after detachment.

An example of this concept is discussed below which was crucial in identifying the different frequency peaks at each operating point. One region was set immediately at the edge of detachment, and the subsequent regions were set as demonstrated on the image on figure 3.5.

A time signal of the gray intensity is recoded which enables us to evaluate the periodicity of the shedding at different operating points. The time difference between each two subsequent images is known ($\Delta t = {}^{1}/_{sampling\ rate}$). Using the average gray level time scale and t, the FFT of the signal was done to get the frequency.

For each operating condition, a total number of around 1 million frames were captured and stored for evaluation. And for each evaluation around 65,000 frames selected at different intervals of the total number of frames. Therefore the length of sampling (number of samples evaluated) is $L = 65000$.

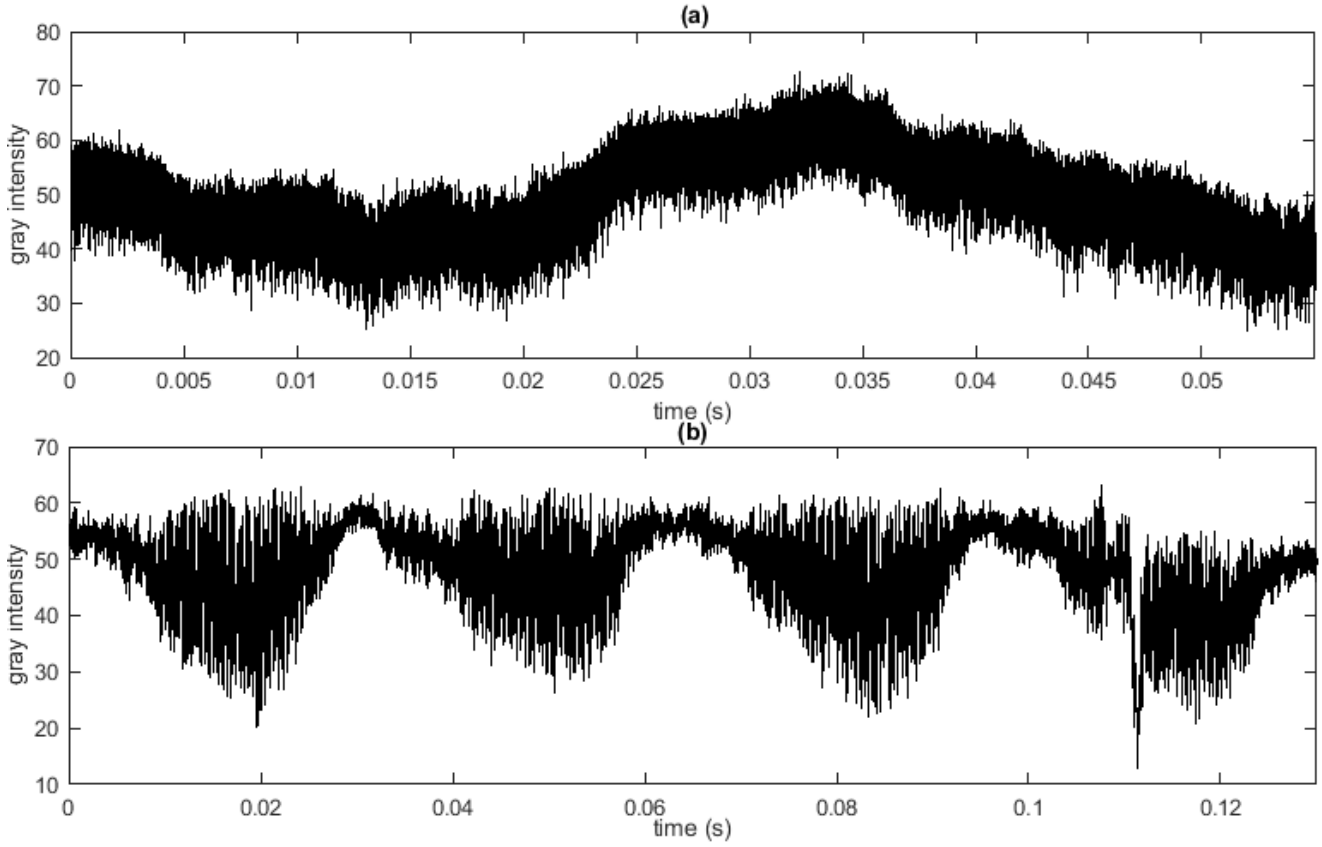

Fig 4.6. The average gray intensity time scale

The two plots (a) and (b) on figure 4.6, compares the averaged gray intensity over time. The time interval used for this analysis is 0.06 s for the parallel throttle and 0.13 s for the converging diverging throttle. The sample rate used was 1 MHz and 0.5 MHz for the two channels respectively. The converging

diverging throttle was averaged over the whole throttle and therefore periodic change in length can be clearly observed from the time vs average gray scale plots above. A smaller ROI was used so as to isolate only the process of cloud detachment. The change in length for the parallel channel is not as distinct relative to the converging diverging channel.

A Fourier Transform is performed to the time signal. The figure 4.6 shows the plot of the FFT Frequency for the time signals derived above.

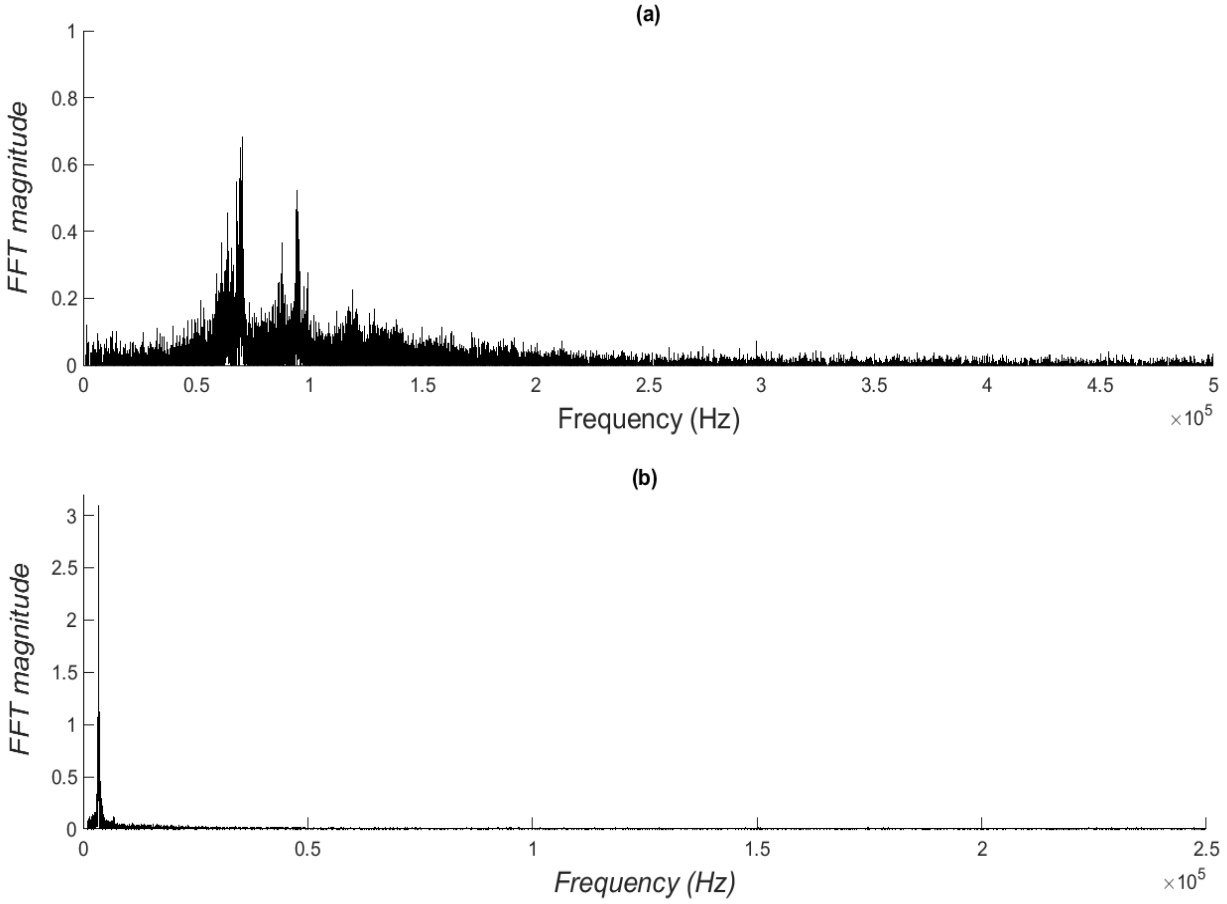

Figure 4.7. The FFT frequency of the gray scale intensity over time. The peaks represent the shedding frequencies. (a) Standard parallel channel. (b) Converging diverging channel.

Two peaks were recorded for the parallel throttle at $F_1 = 69100$ Hz and $F_2 = 94900$ Hz. In the plot the frequency peaks are characterized with a spread of frequency spikes on each side. For each peak the mean frequency was calculated and the resultant standard deviation was found. The standard deviations of $\sigma_{F1} = 1690$ and $\sigma_{F2} = 1700$ respectively. For the converging diverging throttle a peak of $F_1 = 3500\ Hz$ with a standard deviation of $\sigma_1 = 490$.

The analysis shows frequency peaks associated with the cloud shedding. The parallel channel exhibits more than one frequency peaks. The converging diverging channel exhibited one dominant frequency peak.

Focusing on the parallel channel, in most cases two or three frequency peaks were recorded. This phenomenon of more than one peak was not expected, and it was anticipated to be either due to more than one mechanism happening independently therefore having two frequencies. Or the shedding was happening at different frequencies. A visual analysis of the high speed videos suggested that the only other structural change was the length of the cavity oscillation. The length of the cavity is observed to change at a much lower frequency compared to the shedding frequency. And since the frequency peaks seem to be high, and sometimes three or four frequency peaks were observed, therefore the multiple peaks cannot be associated with length oscillation. This was clearly noted in the image analysis approach for the converging diverging channel, where the image shows a periodic change in length, at a low frequency, and subsequently when the length is short, the shedding frequency is high compared to when the length is longer.

To investigate this issue, small portions of the time signal from the average gray intensity were selected and the FFT analysis performed. These portions were with the criterion of length. Therefore, a time signal was evaluated the different lengths of the cavity. The result was a single frequency peak was

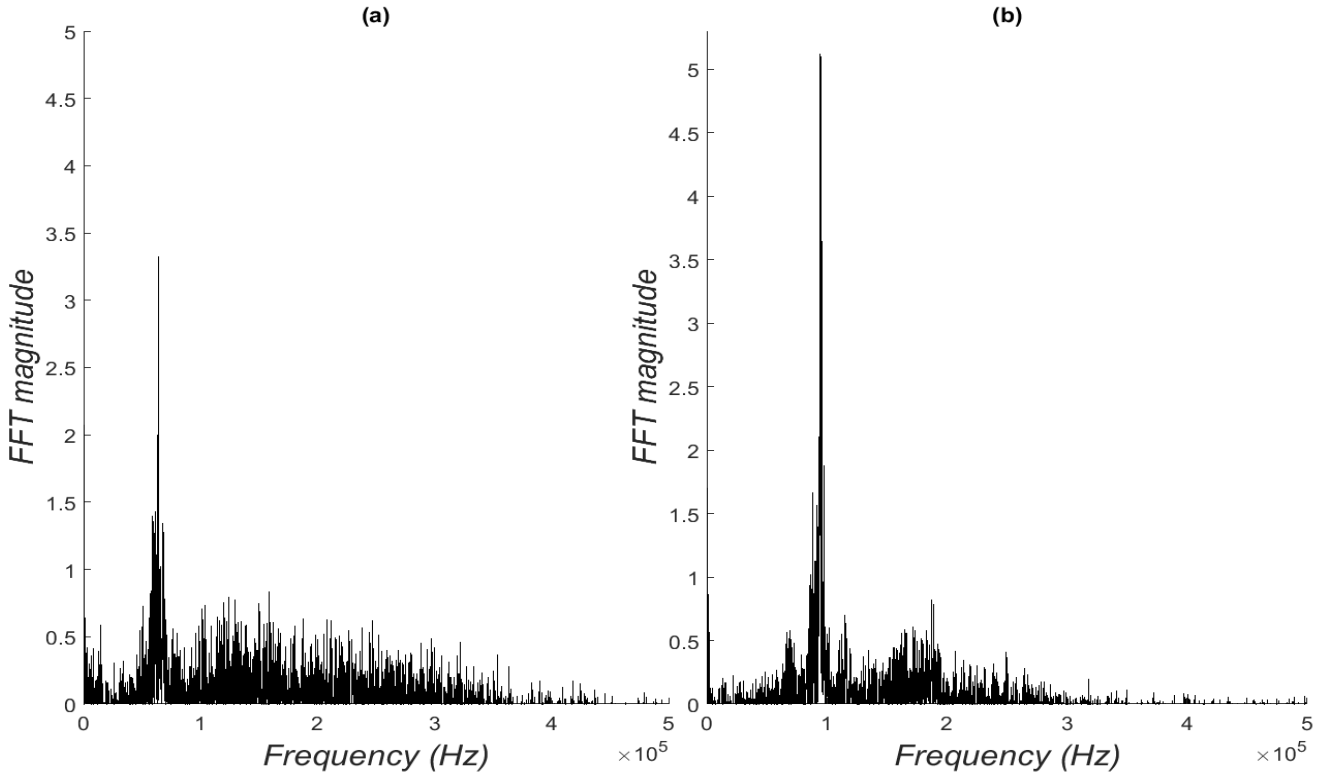

Figure. 4.8. FFT Frequency peaks evaluated at different lengths of the cavity, on the same operating point.

recoded. The frequency peak was the higher frequency peak. The same was done at the interval with longer length, and this resulted to a single lower frequency peak.

In the plots (a) and (b) on figure 4.8, smaller intervals were evaluated when the length is different to demonstrate that the multiple peaks described on the frequency plot on figure 4.6 (a) are associated to the difference in frequency at different length of the attached cavity. During the whole interval used to get the frequency peaks on figure 3.7 (a) the length changes from 0.256 mm to 0.378 mm.

The plot on figure 4.8 (a) on was evaluated at an interval of 0.01 s when the average length of the attached cavity is about 0.3778 mm. Then an interval of 0.012 s was evaluated and the length of the attached cavity is 0.2557 mm and the frequency plot (b) was plotted. Plot (a) has a frequency of $F_1 = 67000\ Hz$ with a deviation of $\sigma_1 = 3010\ Hz$ and length (l_1) of $0.3778\ mm$. The frequency of plot(b) is $F_1 = 93400\ Hz$ with a deviation of $\sigma_2 = 4000\ Hz$ and the length of the attached cavity was $l_2 = 0.2557\ mm$. The two peaks correspond to the frequency peaks observed on the plot (b) on figure 4.7 (a).

Thus every frequency peak is associated to a certain length of the cavity. The length of the cavity was affected by minor instabilities from the pressure generator pumps. Even minor instabilities will change the cavitation number of the flow and as it will be discussed in the following chapters, small changes in cavitation number leads to change in length.

5 PRESSURE INFLUENCE IN CAVITATION

To investigate the effect of pressure on the shedding frequency and cavity behavior, tests were done varying the inlet pressure and keeping the inlet temperature constant and the controlling the cavitation number. The pressure generator set up was used to set gradual increments of the inlet rail pressure from 0 bars to 2200 bars. To further test the effect of P_{in} and what the geometry might have influence on, the three channels mentioned in the previous chapter were used in this experiments.

The pressure drop between the inlet rail pressure and the back pressure is expected to have some effects on the cavitation regimes and ultimetely the behavior of the cavity structures. Keeping the back pressure constant while increasing the inlet rail pressure, would cause a rapid increase in pressure drop (Δp). Consequently, the flow would develop from partial cavitation to supercavitation regime. A control of the cavitation number was necessary so as to keep the cavitating flow at the partial cavitation regime. Tuning the cavitation number and maintaining the length of the cavity at about $1/3$ of the total length of the channel was necessary to isolate only the effect of the inlet pressure. Adjusting the back pressure was done with a manual valve. Both attached cavity length and detached cavity size (diameter) was observed to increase with increase in the inlet pressure when in the partial cavitation regime. The breaking off point was shifted downstream as the inlet pressure was increased. The frequency peaks for each operating point were recorded and plotted against the inlet rail pressure.

The inlet temperature was kept at room temperature. However, the measured outlet Temperature seemed to increase slightly with a maximum increase of 6 ℃. This is obvious due to the compression work done to increase the pressure.

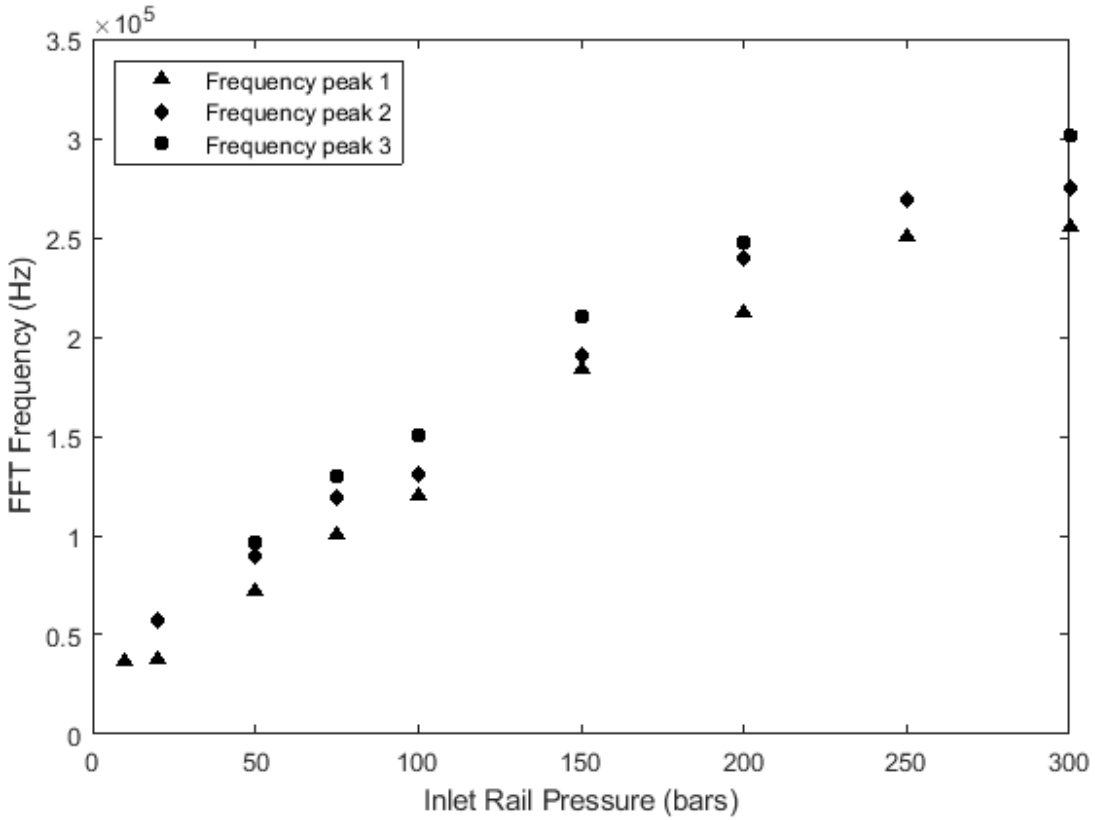

Figure 5.1. Pressure influence on the shedding frequency for a 0.3mm parallel channel.

Figure 3.9 represents the plot of the shedding frequency against the inlet pressure. The fuel used for this measurement was Calibration fluid. The cavitation number was adjusted between (0.75 – 0.81). The mean length of the attached cavity for this set of measurement was ranged between 0.29mm – 0.39mm. At low pressures (Pin < 20 bars), a higher cavitation number of $\sigma \approx 0.8$ was required for the flow to get from non-cavitating flow to partial cavitation regime compared to the cavitation number of ($\sigma \approx 0.73$) at which the regime of the flow was already at partial cavitation regime for Pin > 20 bars . The rest of the operating points in this set of measurements were kept at cavitation number of 0.75 – 0.76. For each operating point, the mean length was recorded. As described in the previous chapter, the attached cavity length has an oscilation and the effect of this is the multiple frequency peaks.

For each inlet pressure variation measurement taken, the mean length of the attached cavity at the point of detachment was recorded. This was the length used in to calculate the strouhal number. The mean length was noted to increase with increase in the inlet pressure from 0.29 mm to 0.39 mm. The velocity of the fluid was calculated by considering the recorded mass flow rate of the fuel and the cross sectional area of the now reduced channel due to the cavitation structure. Therefore, the height used for velocity

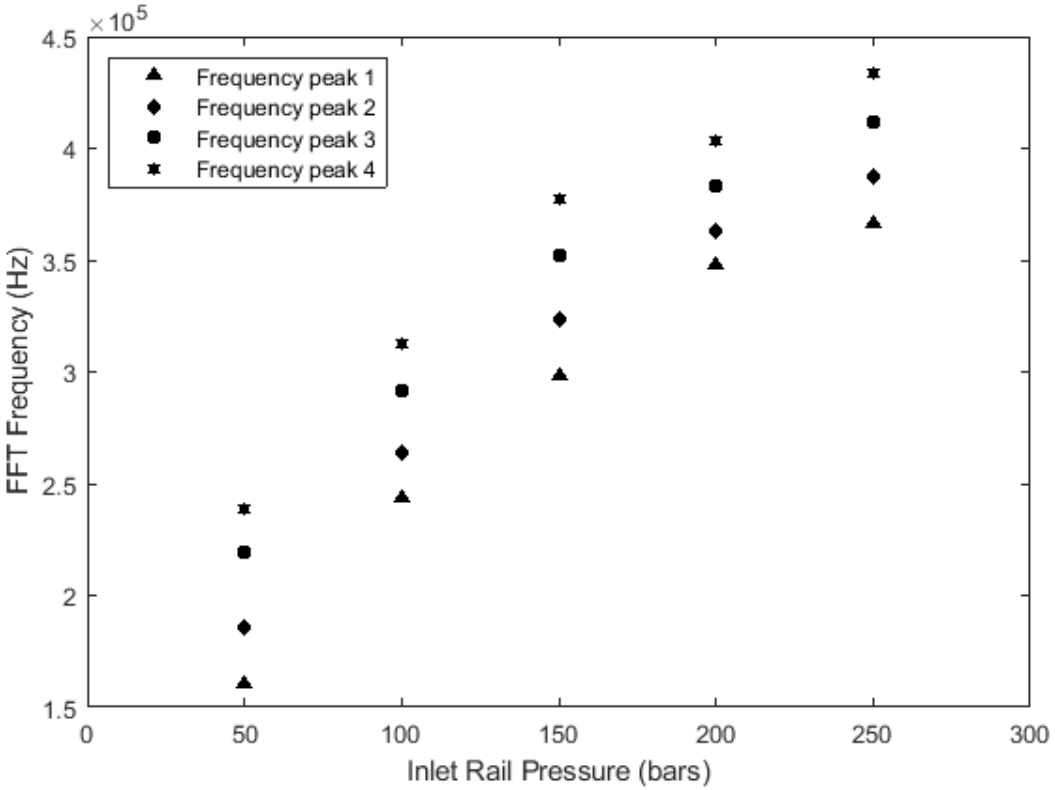

Figure 5.2. Pressure influence on the shedding frequency for a 0.15 mm parallel channel. Fuel used is Calibration fluid

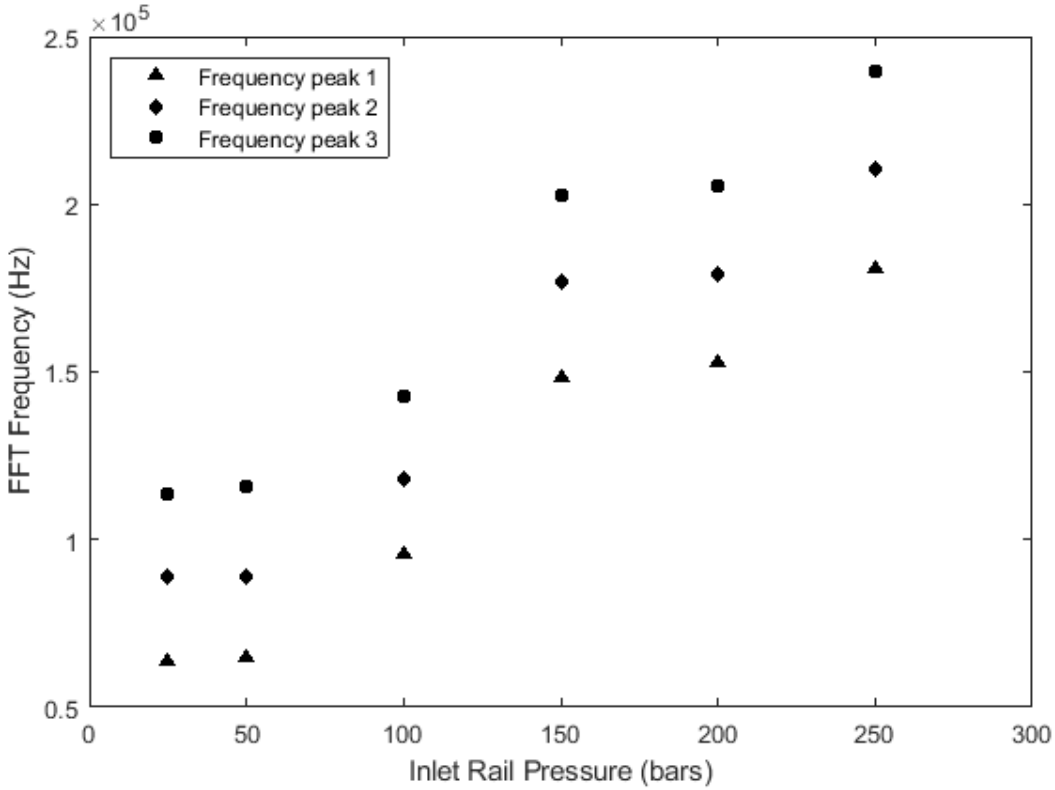

Figure 5.3. Inlet pressure effect on the shedding frequency with dodecane fuel.

calculation was not the height of the channel, rather the height at the neck caused by the cavity structure at the channel. The velocity calculated increased non linearly from 24 m/s to 306 m/s.

Figure 5.1 represents the frequencies for a set of measurement, where the *channel 2* with a height of 0.15mm was used. The temperature was kept at room temperature and then the inlet rail pressure was increased by increments of 50 bar from 0 – 300 bar. Fuel used is calibration fluid 4113. Cavitation number was kept at a constant range of (0.82 – 0.83).

The length of the attached cavity The mean cavity detachment length increased from 0.13 mm to 0.24 mm. Worth noting, the detachment length reduces significantly with the 0.15 mm throttle compared to the 0.3 mm channel. The velocity of the liquid fuel at the constriction due to the cavity structure increased from 63 m/s at 50 bar to 270 m/s at 250 bar.

Figure 5.2. Pressure influence on the shedding frequency of cavitating flow through a parallel channel with height of 0.3 mm. Dodecane fuel was used for this set of experiment. The inlet temperature was kept at room temperature (298 K). Cavitation number was kept constant at 0.76. At low inlet rail pressure (P_{in} < 50 bar), the mean detachment length increased from 0.32 mm to 0.36 mm but negligible difference in shedding frequency was recorded. The velocity however increased from 57 m/s to 84m/s. The maximum velocity at P_{in} = 250 bar is 260 m/s. Test made with dodecane at a room temperature.

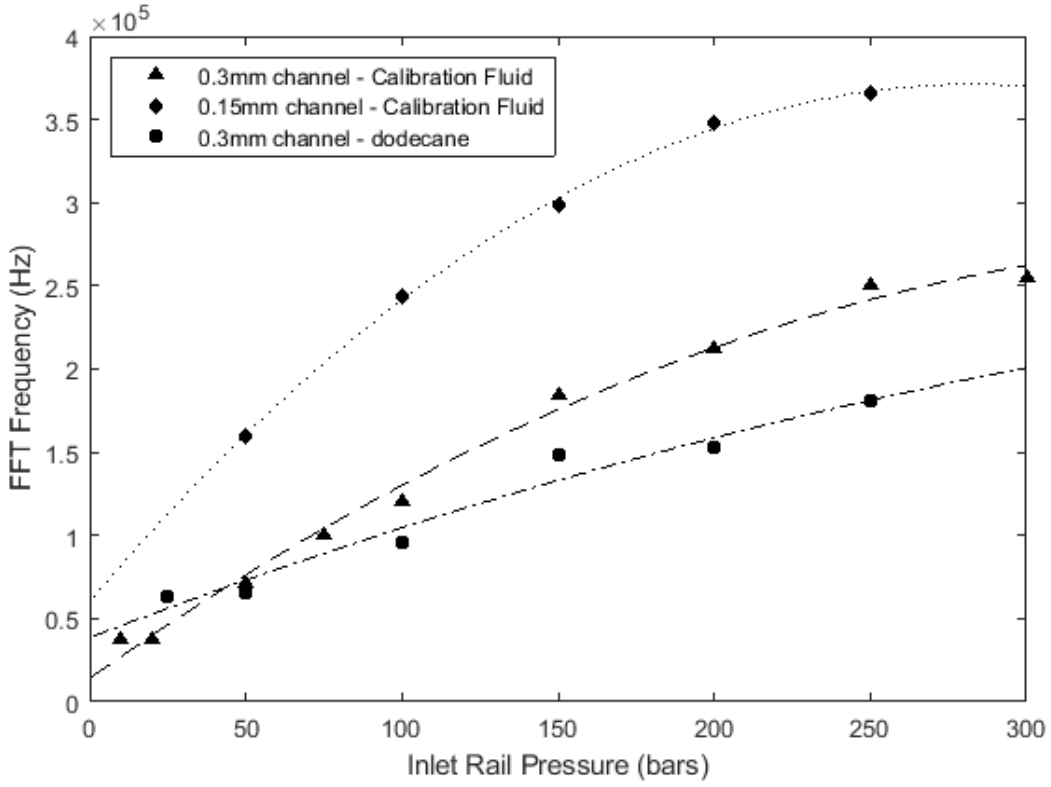

Figure 5.4. Comparison the pressure effect on the frequency with different fuel and geometry of the throttle.

Figure 5.4 compares the effect of change in cross sectional area and the fuel on the shedding frequency. The frequency peak with the highest magnitude for each of the three set of measurements was used to plot the curves. As can be observed on the curve, inlet pressure increase has a non-linear increase, but with a decreasing rate at high inlet pressures.

Comparing the effect of a reduced cross sectional area, the plot shows the frequency significantly increases with the reduction in the height of the parallel throttle from 0.3 mm to 0.15 mm. An almost constant frequency difference (Δf) of $\approx 90\ kHz$ is observed all through the curves of the two channels, with the operating properties kept the same. Comparing the two fuels, both tested at the standard 0,3mm micro channel, there is a notable increase in the shedding frequency with calibration fluid compared to dodecane as we approached higher pressures (Pin > 150 bar).

At pressures lower than 150 bar there is no notably large difference in the shedding frequency between dodecane and calibration fluid. This results can be interpreted that the fuels used had little to no effect on the shedding frequency in a standard channel and the other parameters constant. The increase in the difference in the shedding frequencies at higher pressures in the calibration fluid and dodecane in a standard channel is proposed be due to the change in the chemical properties of the fuels at extreme conditions.

5.1 STROUHAL NUMBER AND REYNOLDS NUMBER

To further characterize the flow and the behavior of the cavitation, the Reynolds number is calculated as shown on equation (1.13). Essentially the Reynolds number is the ration of the inertial to viscous forces in the flow, and characterizes the turbulence of the flow.

To understand the precise relationship between the shedding frequency and the mean velocity (v), which is also affected by the diameter of the flow (h), the two dimensionless parameters were ploted for the sets of measurements described above.

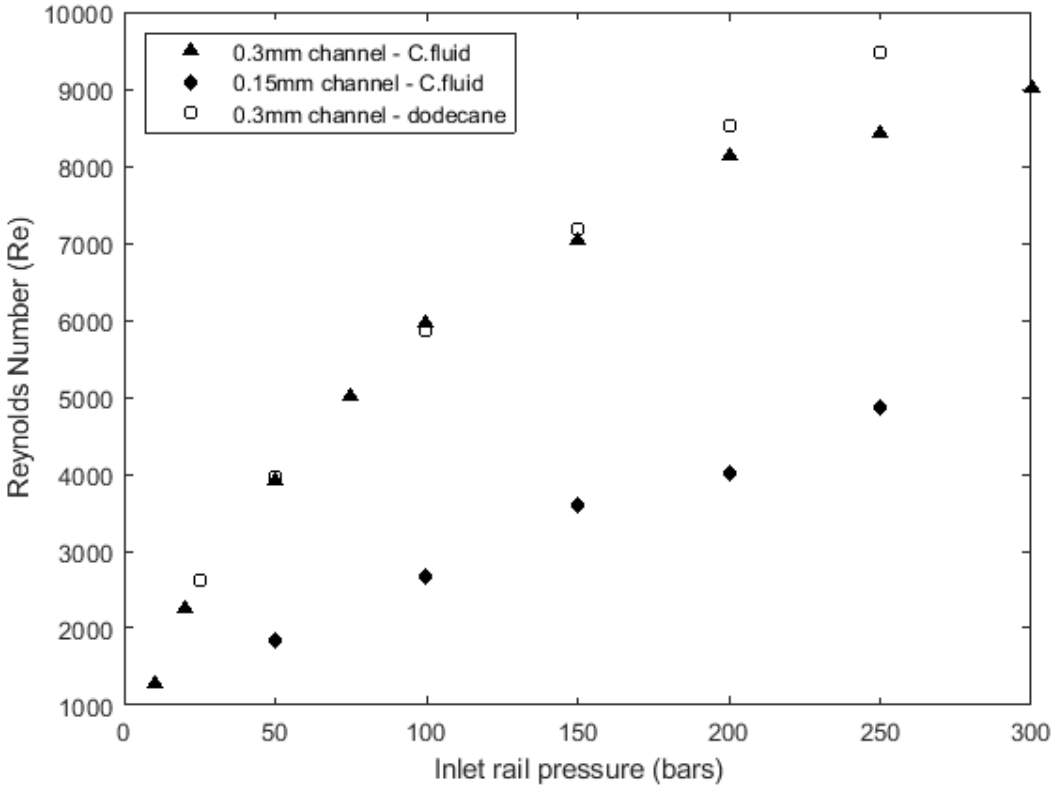

Figure 5.5. The inlet rail pressure plotted against the Reynolds number.

From the plot on figure 5.5, the Reynolds number increases non linearly with the increase of the inlet pressure. This is the expected result that the inlet flow conditions will have a direct effect on the type of flow in the channel, determining whether the flow is laminar or turbulent, thus the Reynolds Number. of course the Reynolds number is a function of the velocity, increasing with the velocity.

To understand the effect of flow properties i.e laminar or turbulent flow, a plot of the Reynolds Number against the Strouhal number has been plotted on the figure 3.14.

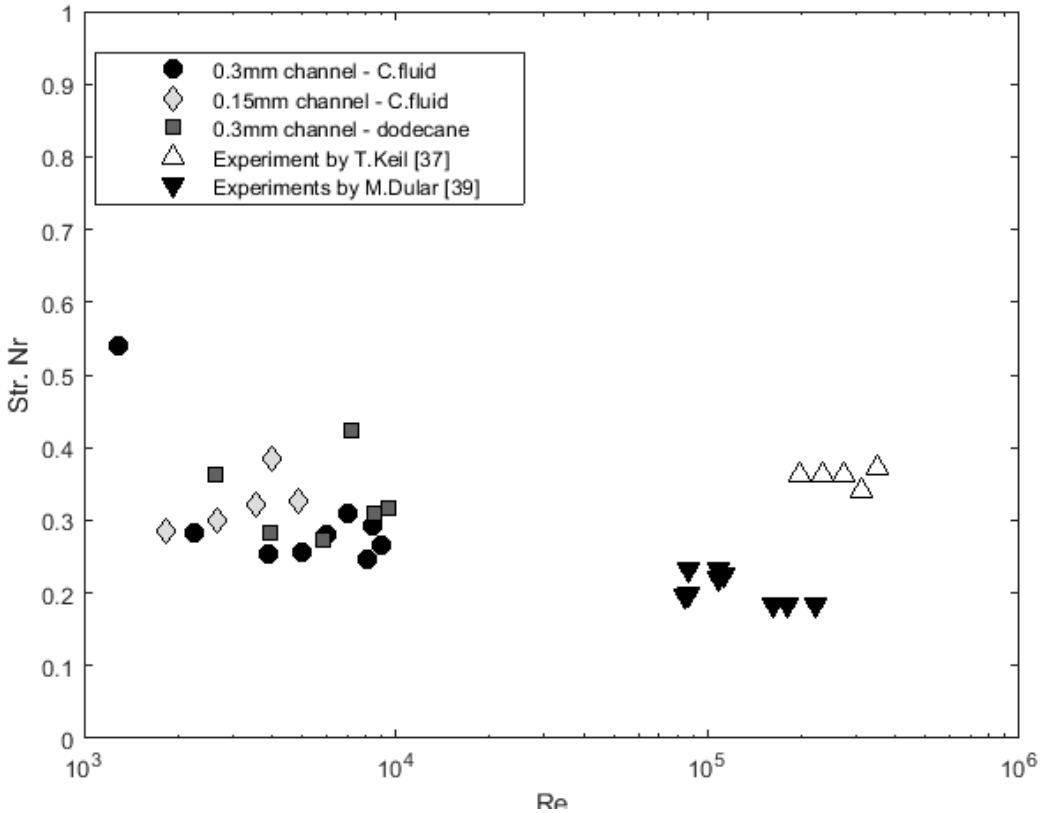

Figure 5.6. Reynolds Number and the Strouhal Number.

The Strouhal Number found in our experimental cases agrees perfectly with the classic range of strouhal numbers (0.2 - 0.4) found by past experiments and is almost constant with mean and standard deviation shown in the table below:

	Mean Str. Nr	deviation
0.3 mm channel – C.fluid 4113	0.303	0.08
0.15 mm channel – C.fluid 4113	0.323	0.03
0.3 mm channel - dodecane	0.328	0.05

Table 5.1. Strouhal Number and the standard deviation for different pressure variation tests

Figure 5.6 compares the strouhal numbers found in this set of experiments described above with the ones found in literature through similar experimental works. The data in figure 5.5 suggests that the Strouhal number is not a function of the geometry nor the fuel or liquid properties. According to past experimental researchers like the experimental study by T. Keil [37] and M. Dular [39], the strouhal

number is not function of the Reynolds number. This is confirmed on the plot on figure 3.14 where a comparison of the Strouhal number for our range or Reynolds number ($2 \times 10^3 - 1 \times 10^4$) and that of very high Reynolds numbers done in the mentioned research is done. In the regime of transition from sheet cavitation to cloud cavitation, past research places the Strouhal number between 0.15 – 0.18.

A critical Reynolds number was also identified below which the cavitation regime is only sheet cavitation without cloud shedding. In this set of experiments, the regime was kept at partial cloud cavitation and thus the critical Reynolds number was not identified.

Therefore, an assertion can be made that the turbulence intensity of the flow has minimal to no influence on the vorticity of the or the shedding frequency of the cavitation. This is true for the same cavitation regime, and cannot be confirmed if the cavitation regime changes.

6 CAVITATION NUMBER EFFECT ON SHEDDING FREQUENCY

To investigate the effect of back pressure on the cavitation behavior, a set of measurements were done setting the inlet pressure constant and adjusting the back pressure with a manual valve mounted downstream the test section. Pressure and temperature sensors located upstream and downstream the test section were used to record the intensive properties of the flow. Then high speed videos were recorded at frame rate ranging from 500 kHz to 1 MHz. Three sets of experimental measurements were made using calibration fluid and one with dodecane.

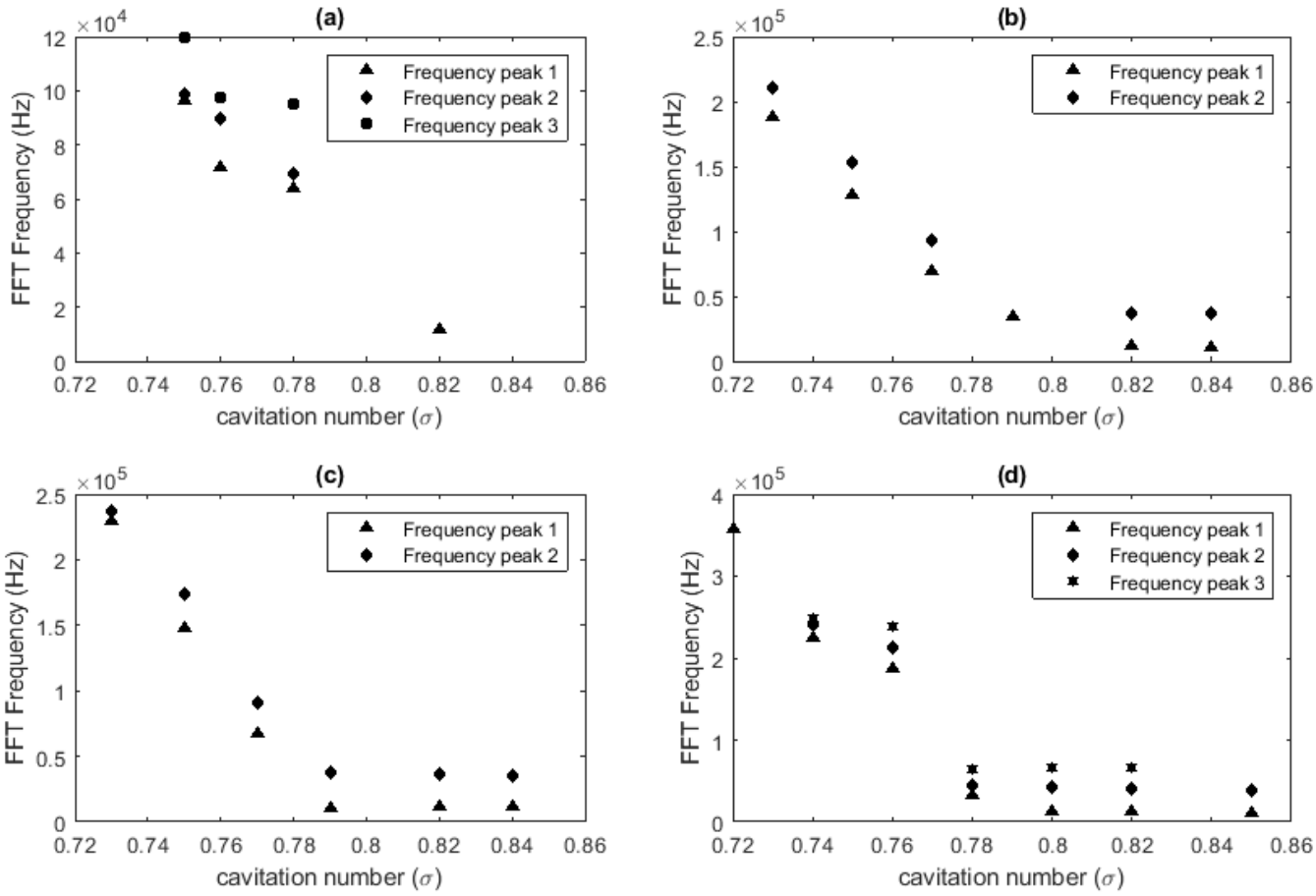

Figure 6.1. Correlation between cavitation number and shedding frequency of the flow.

Figure 6.1 represents (a) Calibration Fluid operating at Pin 50 bar at room temperature. (b) Calibration fluid at Pin 100 bar at room temperature. (c) Dodecane operating point of Pin 100 bar at room temperature. (d) Calibration fluid operating at Pin 200 bar at room temperature.

The set of measurements represented on the plots were carried out by setting the inlet pressure and then gradually increasing the ΔP by means of a valve. The inlet pressure was kept constant. A decrease in the shedding frequency is observed with increase in the ΔP. A steady gradient drop in the shedding frequency is noted at the partial cavitation regime ($\sigma < 0.8$). At the supercavitation regime ($\sigma > 0.8$) the gradient of the curve is almost zero. The shedding frequency change drops with $\approx 90\%$ from the highest frequency that we were able to evaluate at cavitation number (≈ 0.73), to the initial super cavitation regime ($\sigma \approx 0.8$). Also it can be noted from figure 3.15, it was possible to evaluate the frequency at lower cavitation number as we raised the inlet pressure. Therefore, as the inlet pressure is increased, manifestation of periodic shedding was observed at lower cavitation number, compared to lower inlet pressure which required higher cavitation number.

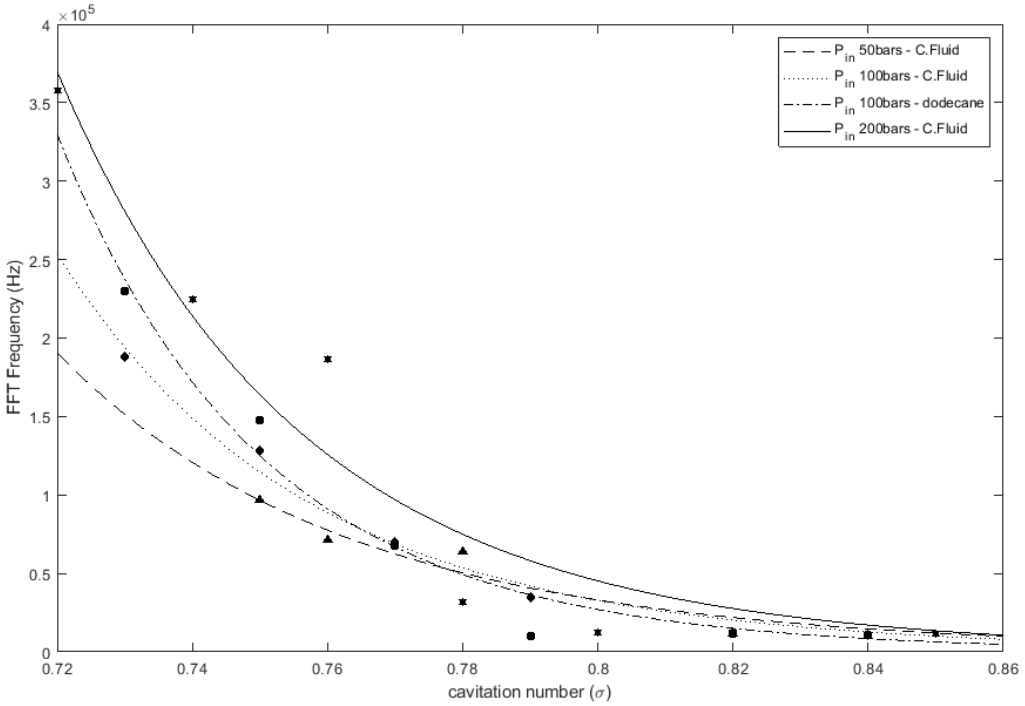

Figure 6.2. Plots of the effect of cavitation number on the frequency keeping the inlet rail pressure constant.

Figure 6.2 further helps to understand the correlation between the cavitation number and the shedding frequency for the different operating points. The high speed videos on the different operating points further showed that when inlet pressure remains constant, the cavitation distribution area of the attached cavity and the diameter of the detached cavity diminishes gradually and even disappeared as back pressure increases. However, this has the inverse effect on the shedding frequency which counterintuitively increases with a drop in ΔP. It therefore can be asserted that high back pressure conditions inhibit the occurrence of cavitation.

Shedding frequency was minimally affected by further drop in the back pressure after getting to the supercavitation regime. It was also noted that the cavitating flow at supercavitation regime is characterized by a lot of noise in the shedding frequency. Therefore, the quality of periodicity of the shedding seemed to reduce at super cavitation regime.

6.1 CAVITATION NUMBER AND THE STROUHAL NUMBER

To compare the effect of the cavitation number on the oscillation behavior of the cavity, the Strouhal number has been plotted against the cavitation number.

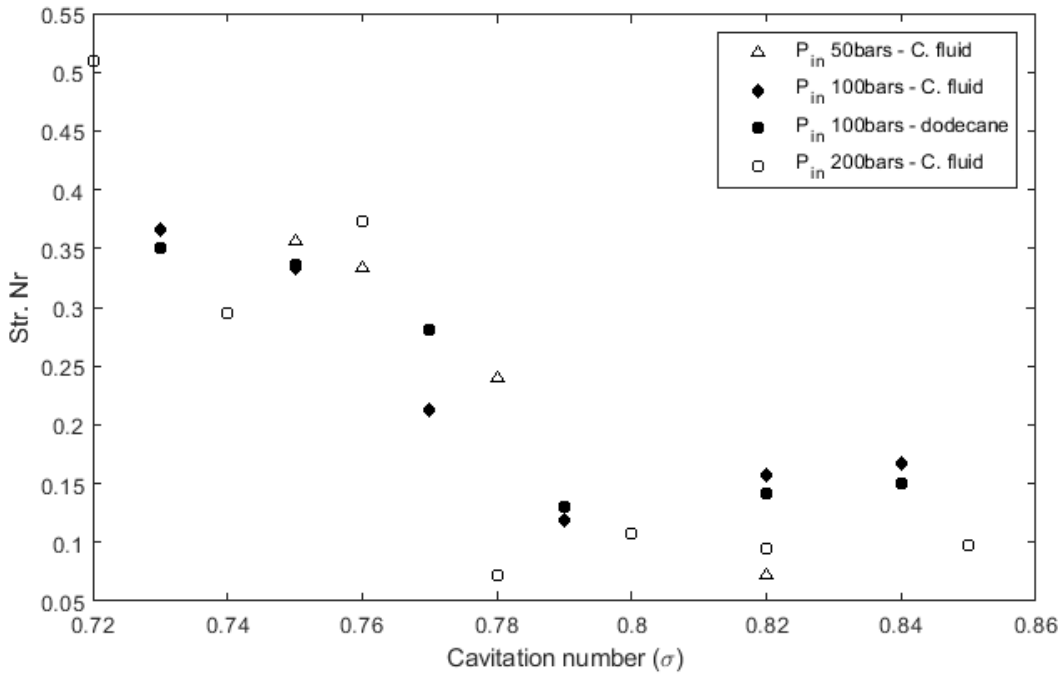

Figure 6.3. Strouhal number for the different cavitation numbers

Figure 6.3 represents the evolution of the Strouhal Number with different cavitation numbers for the four test cases discussed above. The Strouhal number was calculated with the most dominant (highest amplitude) shedding frequency peak among the recorded peaks, and the mean length of the attached cavity. A global trend of the Strouhal Number can be observed which seems to be independent of the inlet pressure and the fuel. According to the trend of the Strouhal number on figure 6.3, a postulation can be asserted that there are two characteristic flow regimes. For cavitation number ($\sigma < 0.77$), the Strouhal number has an almost flat scatter distribution ranging between 0.25 and 0.37. This agrees with the classic value of the Strouhal Number found in the previous section (see figure 3,14) and also from previous researches [37],[38],[39]. For cavitation number ($\sigma > 0.79$) the Strouhal number seems to be unaffected by further increase in the cavitation number, ranging between 0.08 and 0.18. This agrees perfectly with previous experimental work done by William H.[38] and also the findings by T. Keil [37].

However, in the work by T. Keil [37], two flow regimes were investigated, sheet cavitation without cloud shedding, and then with increase in the cavitation number the flow transitions to patial cavitation regime with cloud shedding. In the sheet cavitation regime, the length oscillation was used to calculate strouhal number. A strouhal number of ≈ 0.12 was found for the sheet cavitation and for the partial cavitation with periodic shedding, a Strouhal number in the range of 0.3 - 0.45 was recorded. In this cavitation regime, the Strouhal number found by T.Keil agrees with the one plotted on figure 6.3.

The cases plotted on figure 6.3 were done with the standard parallel channel (channel 1). The dissimilarity of the plot on figure 6.3 with the results found by P.F. Pelz [37], is that for the test cases presented above, there was no observation of sheet cavitation before partial cavitation. Using the standard parallel microchannel, the flow regime transitioned from non cavitating to partial cavitation with cloud shedding. Therefore, the Strouhal number for our study was evaluated from partial cavitation regime to supercavitation regime. As described above, the two characteristic flow regimes observed from the plot on figure 6.3 represent partial cavitation and supercavitation. A transition point from partial cavitation to supercavitation can be identified.

7 TEMPERATURE INFLUENCE ON CAVITATION

A thorough understanding of the thermal effect on cavitating flow is crucial in understanding how this translates to temperature effects on erosion. Similar tests to the ones done to investigate the effects of cavitation number and inlet pressure were carried out to visually study the behavior of cavitation under different temperature of the fuel. The three heat exchangers shown on the schematic of the rig on figure 3.4 were used to vary the inlet temperature of the fuel. The heat exchanger downstream the test section was used to cool the fuel. Inlet pressure was kept constant.

The discussion of the tests done will be divided into two sets of measurement results. In one set of measurements, the cavitation number and the length of the cavity was regulated to keep the flow in the partial cavitation regime. Therefore, there was no transition of cavitation regimes. This was necessary to investigate the effect of temperature on only the shedding frequency. In the second set of measurements, the cavitation number was kept constant and only the temperature was varied.

7.1 TEMPERATURE INFLUENCE ON SHEDDING FREQUENCY

Temperature was varied from $8°C - 130°c$ with calibration fluid and dodecane fuel. Time resolution was done by using a high image acquisition rate of 800,000 – 1,000,000 fps. The high speed video enabled the evaluation of the shedding frequency and a deeper understanding of the behavior of the flow as the temperature is varied. All the tests for temperature variation were taken with the standard throttle with height 0.3 mm.

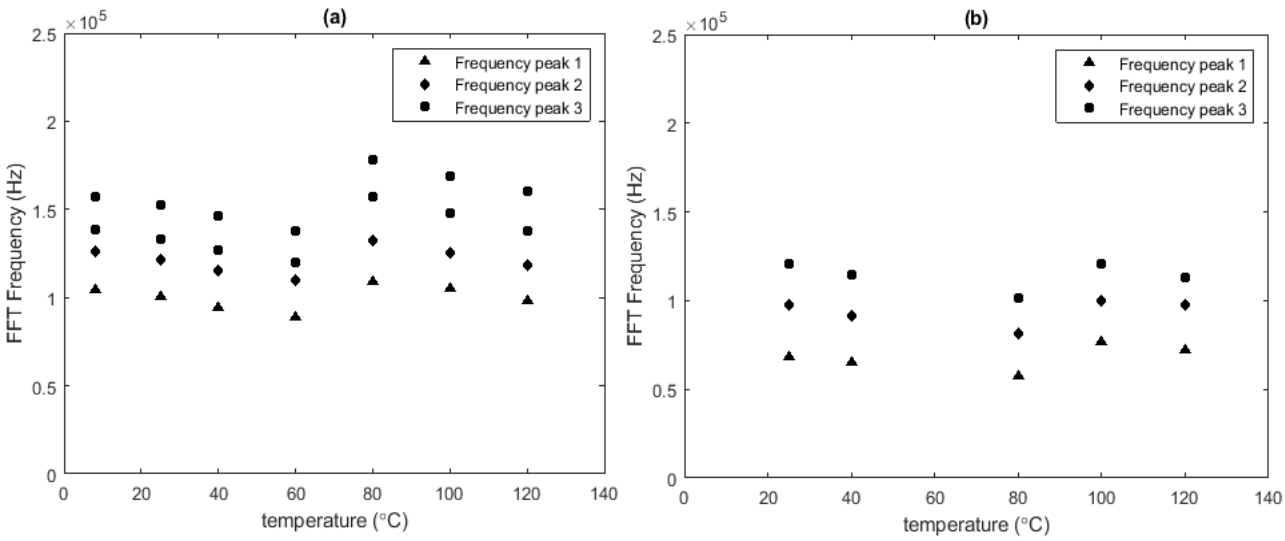

Figure 7.1. Temperature and the shedding frequency for: (a) P_{in} 100bars with Calibration fluid 4113. (b) P_{in} 50 bar with Calibration fluid 4113.

Figure 7.1 represents the plot temperature effect on the shedding frequency. Plot (a) is the results for tests with calibration fluid at an inlet rail pressure of 100 bar. Plot (b) represents tests done at inlet rail pressure of 50 bar and the fuel used was calibration fluid. The several frequency peaks observed in the FFT evaluation have been plotted. In all the cases the length attached cavity was observed to increase with increase in the temperature. Therefore, as stated, for the set of measurements plotted on figure 7.1, the cavitation number was adjusted on the basis of the cavity length. For the plot (a) of figure 7.1, temperature was varied from $8°C - 120°C$. The back pressure was adjusted to keep the cavitation number in the range $0.73 - 0.76$. This range of cavitation number maintained the cavitation regime at the partial cavitation regime. This isolated the effect of temperature on shedding frequency without any superposition of regime transition. The mean length of the attached cavity for this range of cavitation number varied in the range $0.4\ mm - 0.48\ mm$. As the plot (a) on figure 7.1 shows, the shedding frequencies had an evenly flatly scattered trend.

The plot (b) of figure 7.1 represents tests carried out with inlet pressure of 50 bar with calibration fluid. Temperature varied between $25\ °C - 120\ °C$. The cavitation number in this set of measurements was adjusted in the range of $0.73 - 0.75$, and resultantly, length of the cavity varied in the range of $0.25\ mm - 0.55\ mm$. This range is the partial cavitation regime.

Apart from the increase in the length of the attached cavity with rise in temperature, which was observed in the results discussed in the next section, it can be observed that in both tests (figure 7.1 (a) and (b)), temperature didn't depict any immense change in the shedding frequency.

7.2 TEMPERATURE INFLUENCE ON TRANSITION OF CAVITATION REGIME

The dominant effect of temperature on cavitation was the transition of the cavitation regime from partial cavitation to supercavitation. To investigate this, two sets of tests were done, the approach taken was setting the cavitation number constant at 0.76. Therefore, the inlet pressure and the back pressure was unaltered and only the temperature was increased gradually. At each temperature increment step the shedding frequency was evaluated and the length of the attached cavity was recorded.

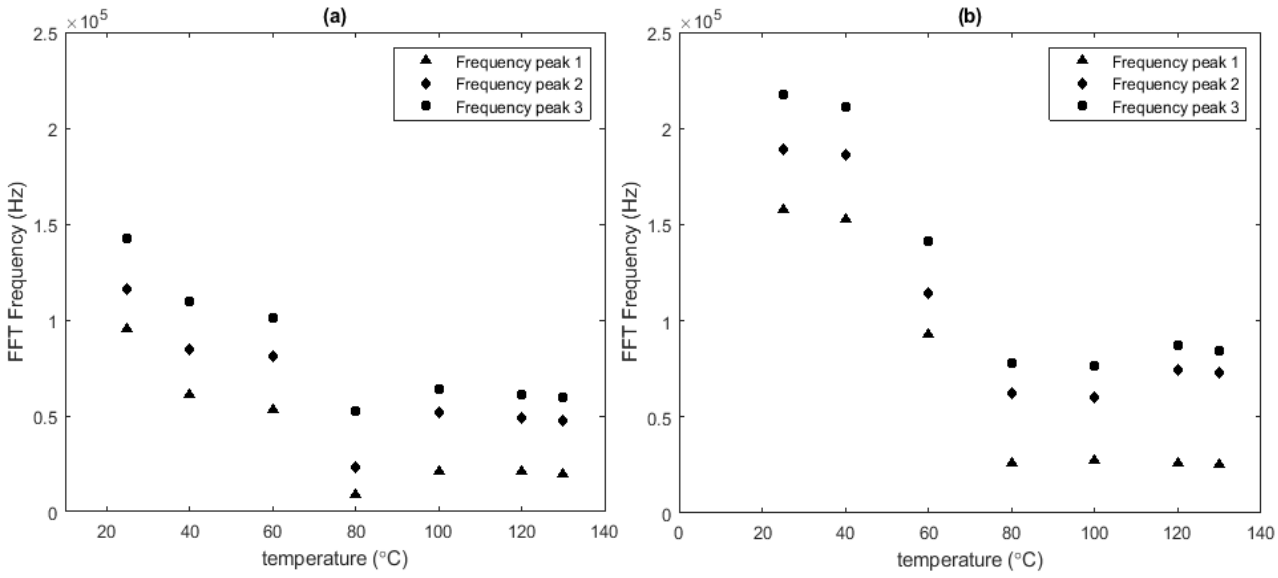

Figure 7.2. Temperature vs Shedding frequency. (a) 100 bar with dodecane. (b) P_{in} 200 bar with Calibration fluid.

Figure 7.2 plot (a) and (b) represent the results of tests done by keeping the ΔP constant at cavitation number of 0.76. Plot (a) represents temperature vs shedding frequency of tests with P_{in} 100 bar with dodecane fuel. Plot (b) represents the temperature vs shedding frequency with P_{in} 200 bar for calibration fluid. Both plots exhibit a similar trend, where the shedding frequency is decreasing as temperature of the two fuels is raised up to a certain transition temperature, after which the shedding frequencies seem to be unaffected anymore by further increase in temperature. Comparing plot (a) and plot (b), for

temperatures below $80\,°C$, a distinct difference in frequency of $\Delta f \approx 60{,}000$ can be observed. Of course this is expected because of the difference in the inlet pressures and the fuels used are different.

However, the frequencies of the two plots seem to converge at higher temperatures ($T > 80\,°C$ in both plots), and this is due to transition to supercavitation. This then leads to two postulations. First, that the dominant effect of temperature increase on the cavity behavior is transition to supercavitation regime. Secondly, that the transition temperature is independent of the inlet pressure and, going by these two test cases, also this temperature is the same for both dodecane and calibration fluid. More tests must be conducted to confirm with precision that the transition temperature is not a function of fuel.

The transition temperature was also validated by the length plot below which showed a jump rise at 80 ℃.

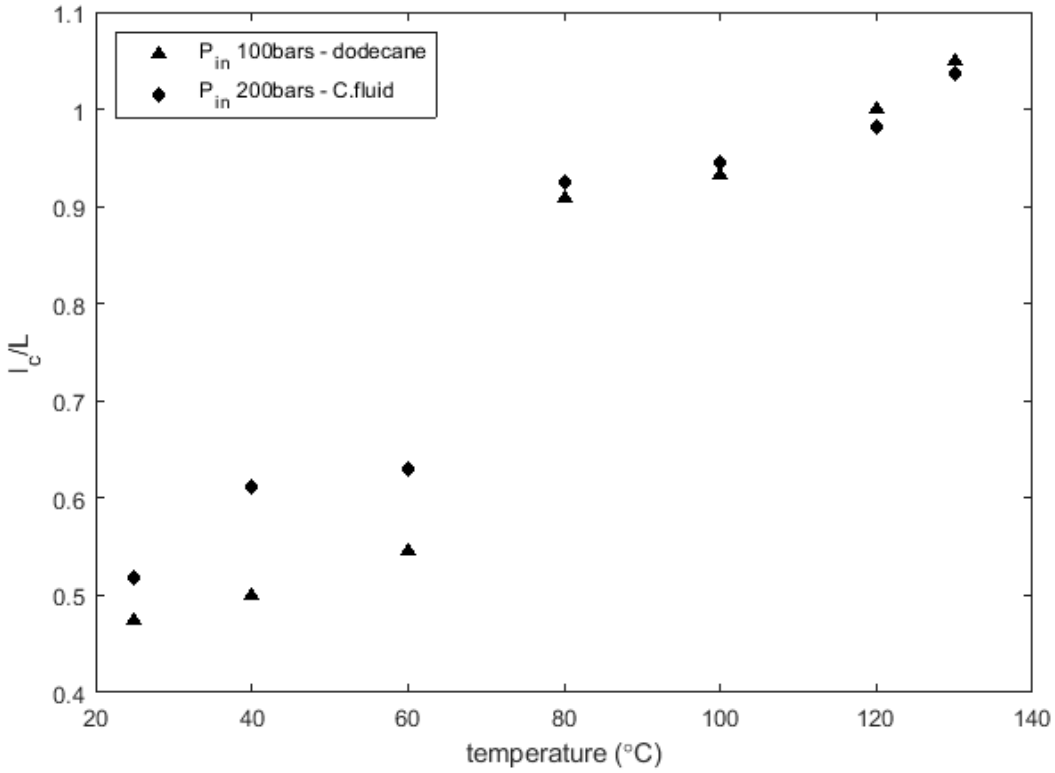

Figure 7.3. Temperature influence on the length of the sheet cavity

Figure 7.3 represents the normalized length of the cavity plotted for the two temperature variation tests mentioned above. The plot shows for temperature below the transition temperatures ($T < 80$ ℃), both experiments, done with P_{in} 200 bar and P_{in} 100 bar exhibit a gradual, almost linear, increase in length.

Also noteworthy, in the partial cavitation regime the length of the cavity is a function of the inlet pressure. This is evident since the normalized length for P_{in} 200 bar is more compared to P_{in} 100 bar before the transition of the cavitation regime.

Cavitation regime transition is characterized by the jump increase in normalized length. This transition temperature agrees with the one observed on figure 3.15 with the frequency vs temperature plot. Notably the mass flow rate also decreases gradually and steadily with increase in temperature in all test cases. This can be attributed to the decrease in the density as the temperature is raised.

8 CONCLUSION

Cavitation was investigated in micro channels with rectangular cross section. Different inlet and out-flow conditions under different geometrical channels and different fuels were applied. A lot of experimental research has been done on cavitation behavior on hydrofoils but there is a lack of vast knowledge on cavitation behavior in microchannels. Perhaps this is due to the complexity associated with data collection in micro scale geometries. This has led to more investigations on the effects of cavitation like erosion rather than the mechanism itself. The investigation assumed 2D microchannels with a thickness of 0.3mm and made of steel, which is a simplified imitation of the cylindrical channels applied for example in injector nozzles. This enabled us to visually access the flow in the channel by placing the plate between two glass windows. High speed visualization technique is used to resolve the temporal and partial scale of the flow in the micro channel. The high speed videos are processed by image processing techniques. Data collected include velocity of the flow and cavity, change in length, reentrant jet motion, the shedding frequencies and size of the cavities.

As expected, there was notable differences in the behavior of cavitation as the inlet pressure was varied. Inlet pressure variation affected the regime type of the cavitation, shedding frequency and the length of the cavity. Initiation of the cavitation mechanism is obviously dependent on the inlet pressure. An increase in temperature led to transition from partial cavitation regimes. The length also increased with increase in temperature and the shedding frequency increases non linearly with inlet pressure. The most dominant effect of inlet pressure was the shedding frequency.

This experimental research also gave more insight to the effects of geometry on cavitation behavior. A parallel channel with 0.3mm height was compared to the 0.15mm height channel. The standard parallel channel (h=0.3mm) and reduced height parallel channel (0.3mm) showed distinct cavitation behavior difference, in terms of the size of the attached cavity, the shedding frequency and the inlet pressure required for the cavitation initiation.

Different set of measurements was done varying the backpressure to understand how the cavitation mechanism changes with change in cavitation number (ΔP). This had the greatest influence on the cavitation regime and length of the attached cavity. Stability of the sheet cavitation is dependent on the ΔP.

Thermal effects on the cavitation phenomena was tested by heating the fuel to temperatures between $8℃ - 130℃$ and keeping the other parameters constant. This was done with Calibration fluid and dodecane fuel. The results for the temperature variation tests showed that the most dominant effect of temperature elevation was the cavitation regime transition. The transition temperature was identified for both fuels. Further investigations are underway to identify if this transition temperature is affected by the pressure and geometry of the channel. The results also concluded that the temperature had little to no effect on the shedding frequency in the same cavitation regime.

Future research will be focused on connecting the cavitation mechanism with erosion phenomena. The thermal effects and particularly thermal delay for which there is vast literature in bubble dynamics field, will be studied in the cloud cavitation field. High speed visualization techniques will be used to take highly time resolved erosion tests simultaneously with the cavity mechanism tests. This will shed light and give a one to one link of cavity behavior and erosion, including cloud collapse.

9 REFERENCES

[1] Brennen, C. E. (1995): Cavitation and bubble dynamics. Oxford University Press, London.

[2] Grist, E. (1999): Cavitation and the centrifugal pump. Taylor & Francis, London.

[3] Knapp, R. T. (1955): Recent Investigations of the Mechanics of Cavitation and Cavitation Damage, Trans. ASME, 77, 1045-1054.

[4] Furness, R. A., (1974): Studies of the Mechanics of Fixed Cavities in a Two-Dimensional Convergent-Divergent Nozzle, Cavitation, I Mech E, C160/74, 119-128.

[5] Pham, T. M., Larrarte, F. and Fruman, D. H. (1999): Investigation of Unsteady Sheet Cavitation and Cloud Cavitation Mechanisms, J. Fluids Eng., 121, 289-296

[6] Le, Q., Franc, J. P. and Michel, J. M. (1993): Partial Cavities: Global Behavior and Mean Pressure Distribution, J. Fluids Eng., 115, 243-248.

[7] Keiichi SATO, Shigemasa SHIMOJO: Detailed observations on a starting mechanism for Shedding of cavitation cloud

[8] Sato, K., Shimojo, S. and Watanabe, J. (2003): Observations of Chain-Reaction Behavior at Bubble Collapse Using Ultra High Speed Video Camera, Proc. of FEDSM'03, ASME, FEDSM2003-45002,1-6.

[9] Jean-Pierre Franc, Jean-Marie Michel: Fundamentals of Cavitation.

[10] Hitoshima SOYOYAMA. Yoshaika YAMAUCHI, ADACHI, SATO, SHINDO, Risaburo OBA: High Speed Observations of the Cavitation Cloud around a High Speed Submerged Water Jet

[11] Matvez DULAR, Strojniški VESTNIK: The Issue Of Strouhal Number Definition In Cavitating Flow

[12] BRENNEN, C. E., 1994, Hydrodynamics of Pumps, Oxford University Press, Oxford, UK.

[13] Juhno KIM, Seung Jin SONG: Measurement of Temperature Effects On Cavitation in a Turbopump Inducer.

[14] Matevz DULAR, Oliver COUTIER-DELGOSHA: Thermodynamic Effects During Growth and Collapse of a Single Cavitating Bubble.

[15] Sheng-Hsueh YANG, Sheng-Yuh JAW, Keh-Chia YEH: Single cavitation bubble generation and observation of the bubble collapse flow induced by a pressure wave

[16] JESHANI, M. (2013): Optical characterisation of cavitating flows in diesel fuel injection equipment. (Unpublished Doctoral thesis, City University London)

[17] Ehsanallah TAHMASEBI: Simulation of internal flow in fuel Injection process.

[18] Knapp, R., Daily, J., and Hammitt, F. (1970) *Cavitation*, New York: McGraw_Hill.

[19] Temperly, H.N.V. (1947): *Proc. Phys. Soc.* vol. 59, p. 199.

[20] Yoshinobu Tsujimoto, Satoshi Watanabe: Cavitation Instabilities of Hydrofoils and Cascades

[21] Keiichi Sato, Shigemasa Shimojo: Detailed Observations On A Starting Mechanism For Shedding Of Cavitation Cloud (Cav03-Gs-4-009)

[22] Chris Willert, Stefan Freitag , Christoph Hassa : High Speed Imaging Using Low Cost Illumination Source.

[23] https://photron.com/uses/laser-illumination/

[24] Pulsed operation of high-power light emitting diodes for imaging flow velocimetry.

[25] Alexander J. Smits: Flow Visualization: Techniques and Examples

[26] Mathew Dirjish: Replacing Laser Diodes With LEDs, And Vice Versa

[27] Patrick H. Geoghegan1, Nicolas A. Buchmann, Julio Soria, Mark Jermy: High-speed LED-illuminated PIV measurements of the time-dependent flow field in a stenosed, compliant arterial model.

[28] Andreas Nolte, Lutz Höring: Fundamentals of illumination sources

[29] Michel Versluis: High-speed imaging in fluids

[30] C. Mauger, L. M_e_es, M. Michard, M. Lance: Velocity measurements based on shadowgraph-like image correlations in a cavitating micro-channel flow.

[31] Hui Cao, Junying Y. Xu, Yong Ling, Alexander L. Burin, Eric W. Seeling, Xiang Liu, and Robert P. H. Chang : Random laser with coherent feedback.

[32] Ezddin A. F. Hutli, Milos S. Nedeljkovic: Frequency in Shedding/ Discharging Cavitation Clouds Determined by Visualization of a Submerged Cavitating Jet.

[33] M. M. Biss, G. S. Settles, M. J. Hargather, L. J. Dodson, and J. D. Miller: High-speed digital shadowgraphy of shock waves.

[35] D. Funfschilling1, G. Castanet2, N. Rimbert2: Turbulent cavitation in a microchannel

[36] C. Stanley, T. Barber, G. Rosengarten: Re-entrant jet mechanism for periodic cavitation shedding in a cylindrical orifice

[37] T. Keil,P. F. Pelz, U. Cordes, G. Ludwig: Cloud Cavitation and Cavitation Erosion in Convergent Divergent Nozzle

[38] Willian Hogendoorn (2017): Experimental investigation of cavitation regimes in a converging-diverging nozzle. Report Number 2817.

[39] Matevz Dular, M. Adama Maiga, O. Coutier-Delgosha: Scale effect on unsteady cloud cavitation,